

Infrared Spectra and Spectral Energy Distributions for Dusty Starbursts and AGN

Lusine Sargsyan¹, Daniel Weedman², Vianney Lebouteiller^{2,3}, James Houck², Donald Barry², Ashot Hovhannisyanyan⁴ and Areg Mickaelian¹

ABSTRACT

We present spectroscopic results for all galaxies observed with the *Spitzer* Infrared Spectrograph (IRS) which also have total infrared fluxes f_{IR} measured with the Infrared Astronomical Satellite (IRAS), also using AKARI photometry when available. Infrared luminosities and spectral energy distributions (SEDs) from 8 μm to 160 μm are compared to polycyclic aromatic hydrocarbon (PAH) emission from starburst galaxies or mid-infrared dust continuum from AGN at rest frame wavelengths $\sim 8 \mu\text{m}$. A total of 301 spectra are analyzed for which IRS and IRAS include the same unresolved source, as measured by the ratio $f_{\nu}(\text{IRAS } 25 \mu\text{m})/f_{\nu}(\text{IRS } 25 \mu\text{m})$. Sources have $0.004 < z < 0.34$ and $42.5 < \log L_{IR} < 46.8$ (erg s^{-1}) and cover the full range of starburst galaxy and AGN classifications. Individual spectra are provided electronically, but averages and dispersions are presented. We find that $\log [L_{IR}/\nu L_{\nu}(7.7 \mu\text{m})] = 0.74 \pm 0.18$ in starbursts, that $\log [L_{IR}/\nu L_{\nu}(7.7 \mu\text{m})] = 0.96 \pm 0.26$ in composite sources (starburst plus AGN), that $\log [L_{IR}/\nu L_{\nu}(7.9 \mu\text{m})] = 0.80 \pm 0.25$ in AGN with silicate absorption, and $\log [L_{IR}/\nu L_{\nu}(7.9 \mu\text{m})] = 0.51 \pm 0.21$ in AGN with silicate emission. L_{IR} for the most luminous absorption and emission AGN are similar and 2.5 times larger than for the most luminous starbursts. AGN have systematically flatter SEDs than starbursts or composites, but their dispersion in SEDs overlaps starbursts. Sources with the strongest far-infrared luminosity from cool dust components are composite sources, indicating that these sources may contain the most obscured starbursts.

¹Byurakan Astrophysical Observatory, 378433, Byurakan, Aragatzotn Province, Armenia; sarl11@yahoo.com

²Astronomy Department, Cornell University, Ithaca, NY 14853; dweedman@isc.astro.cornell.edu

³Laboratoire AIM, CEA/DSM-CNRS-Universite Paris Diderot, DAPNIA/Service d'Astrophysique, Saclay, France

⁴Department of Physics, Yerevan State University, Yerevan, Armenia

Subject headings: infrared: galaxies — galaxies: starburst— galaxies: active—
galaxies: distances and redshifts— galaxies: evolution

1. Introduction

Infrared observations are crucial to understanding the formation and evolution of galaxies, because the most luminous galaxies in the universe are dusty and heavily obscured (Soifer, Neugebauer, and Houck 1987). Most of their primary luminosity arising from optical and ultraviolet luminosity is absorbed and subsequently reradiated in the infrared by the absorbing dust. Three decades of discovery with the Infrared Astronomical Satellite (IRAS), the Infrared Space Observatory (ISO), and the *Spitzer* Infrared Observatory (*Spitzer*) have traced evolution for the most luminous galaxies in the universe to redshift $z \sim 3$ (brief review in Houck and Weedman (2010)).

The epoch with $2 \lesssim z \lesssim 3$ is distinctive because it is the epoch at which the luminosity of optically-discovered sources is observed to peak (e.g. Madau et al. 1998; Reddy and Steidel 2009). It is important to characterize thoroughly all populations found within this epoch. Once that is accomplished, the next frontier is to understand the initial formation of galaxies by studying sources at redshifts $z > 3$. When were the first galaxies with rapid and intense star formation (“starbursts”) and the first active galactic nuclei (AGN)? What fraction of these luminous sources are obscured by dust? When did dust emission become the dominant luminosity in the universe?

For example, it is essential to determine whether optically-discovered sources to $z \sim 8$ observed in the rest-frame ultraviolet (e.g. Bouwens et al. 2009) are the dominant population in the early universe. Dusty galaxies would not be found within such optically selected samples at high redshift because of the very large extinction in the rest frame ultraviolet. Comparison of starburst luminosity in the mid-infrared and ultraviolet rest frames indicates that less than 1% of the intrinsic ultraviolet luminosity emerges from the most luminous infrared-selected sources (e.g. Sargsyan et al. 2010). Does this very large dust obscuration apply to sources in the early universe and prevent optical discovery of the most luminous galaxies? Answers to such questions will be determined by future observations at far-infrared to millimeter wavelengths, where dusty galaxies can be discovered at redshifts $z > 3$.

Mid-infrared spectra are available from the *Spitzer* Infrared Spectrograph (IRS; Houck et al. (2004)) for hundreds of optically-faint infrared sources, including starbursts, AGN, and composite sources with signatures of both. These sources range in luminosity from 10^8 to 10^{14}

L_{\odot} and in redshift from $0 < z < 3$. These sources were discovered in surveys at $24 \mu\text{m}$ with the *Spitzer* Multiband Imaging Photometer System (MIPS; Rieke et al. (2004)) and subsequently observed with the IRS.

Results and source lists for dusty starbursts and AGN are summarized in Weedman and Houck (2008) and Weedman and Houck (2009b). (Because the objective of these summaries was to determine separately the characteristics of starbursts and AGN, composite sources were not included.) Primary sources for spectroscopic results are Houck et al. (2005); Hao et al. (2005); Brandl et al. (2006); Shi et al. (2006); Weedman et al. (2006a,b); Armus et al. (2007); Farrah et al. (2007); Houck et al. (2007); Imanishi et al. (2007); Markwick-Kemper et al. (2007); Sajina et al. (2007); Schweitzer et al. (2008); Yan et al. (2007); Brand et al. (2008a,b); Farrah et al. (2008); Martinez-Sansigre et al. (2008); Polletta et al. (2008); Pope et al. (2008); Sargsyan et al. (2008); Dasyra et al. (2009); Desai et al. (2009); Farrah et al. (2009a); Hernan-Caballero et al. (2009); Haung et al. (2009); Menendez-Delmestre et al. (2009); Weedman and Houck (2009a) and Weedman and Houck (2009b).

These sources provide the available sample of dusty, luminous galaxies extending to $z \sim 3$. To interpret these sources and relate them to future new discoveries, it is necessary to determine how the mid-infrared spectroscopic parameters defining classification and luminosities of starbursts and AGN relate to total infrared luminosities and photometric parameters derived from spectral energy distributions (SEDs). The purpose of the present paper is to compare mid-infrared spectroscopic features with total infrared luminosities and spectral energy distributions (SEDs) for large numbers of sources having available both mid-infrared *Spitzer* IRS spectra and also far infrared photometric results.

This comparison will allow: determining luminosities from mid-infrared spectroscopic parameters; relating local starbursts and AGN to far infrared and submillimeter sources discovered at high redshifts; determining parameters which can distinguish starbursts and AGN, particularly the long wavelength, cold dust component; and determining empirical templates and their dispersion among starbursts and AGN for modeling source counts and source colors within surveys at various far infrared to millimeter wavelengths.

We have two primary objectives for this paper. The first is to determine the total luminosities of sources as a function of mid-infrared spectral features, so that the large numbers of *Spitzer* spectra available for sources with $z < 3$ can be used to determine the total luminosities of starbursts and AGN at these epochs. Our second primary objective is to utilize a consistent mid-infrared spectral classification for sorting objects among starbursts, AGN, and composites, and then to determine median SEDs of these different categories. This will allow a conclusion of how accurately SEDs alone can classify high redshift, luminous sources which are being discovered with far infrared and submillimeter observations.

The spectral features we use for our analysis are simply the localized spectral maxima arising from peak flux densities for the polycyclic aromatic hydrocarbon (PAH) 7.7 μm emission feature in spectra of sources containing starbursts, and the 7.9 μm spectral continuum peak for obscured AGN with silicate absorption. (For unobscured AGN with neither feature, the spectral continuum at 7.9 μm is measured.) Examples are illustrated in Figure 1 to show how such features would appear in observed IRS spectra of sources such as those analysed below if redshifted to $z = 2.5$. Our objective is to measure the strongest features, motivated by using these parameters to have reliable and self-consistent data for the large numbers of sources discovered by *Spitzer* at $z \gtrsim 2$ for which S/N is poor, and deconvolution of the total flux within spectral features is uncertain (Houck et al. 2007; Weedman and Houck 2008, 2009a,b).

Use of these spectral features will allow comparisons of SEDs and source luminosities for our local sample to the samples at $z \gtrsim 2$ with available spectra. These new comparisons can be made because the high redshift sources having *Spitzer* spectra were originally discovered within *Spitzer* survey fields that are now included in mapping to wavelengths of 500 μm in the Herschel Multi-tired Extragalactic Survey (HerMES; Oliver et al. (2010)). SEDs for these high redshift sources can be compared at the same far-infrared rest frame wavelengths included in our local sample (e.g. Rowan-Robinson et al. 2010; Chapman et al. 2010).

To achieve our objectives, we assemble and analyze a collection of 301 sources which have both IRS spectra and IRAS photometry; when available, photometry extending to 160 μm is also used from the AKARI mission (Murakami et al. 2007; Onaka et al. 2007; Kawada et al. 2007; Kaneda et al. 2007). Using this sample, the spectral features from *Spitzer* IRS spectra at rest frame $\sim 8 \mu\text{m}$ are compared to photometric parameters from 8 μm to 160 μm measured with IRAS and AKARI.

Individual spectra of the sources which we discuss in this paper are available electronically.¹

2. Sample Selection and Observations

All sources were observed with the IRS using the low resolution modules Short Low 1 (SL1), Short Low 2 (SL2), Long Low 1 (LL1) and Long Low 2 (LL2), giving spectral

¹Query on source name at <http://cassis.astro.cornell.edu/sargsyan-et-al>; The Cornell Atlas of Spitzer IRS sources (CASSIS; V. Leboutteiller et al. in preparation) is a product of the Infrared Science Center at Cornell University, supported by NASA and JPL.

coverage from $\sim 5 \mu\text{m}$ to $\sim 35 \mu\text{m}$. For all spectra which we analyzed, spectral extractions were done with the SMART analysis package (Higdon et al. 2004), using the improved "optimal extraction" procedure in Leboutteiller et al. (2010)².

The optimal extraction procedure fits an empirical point spread function (PSF) for an unresolved source to the spectral image and weights each pixel in the image according to its fraction of illumination by the source. This reduces the noise arising from the background. Spectral flux calibration is provided using observations of standard stars; this calibration corrects for slit losses for unresolved sources. The flux calibration is correct to within $\sim 5\%$ for unresolved sources. For resolved sources, the fitting of the PSF and finite slit size results in an underestimate of the flux density in the extracted spectrum.

Our objective is to compare spectral features from the IRS with overall spectral energy distributions (SEDs) determined photometrically to far infrared wavelengths using IRAS and AKARI. To make such comparisons, it is necessary to use only unresolved sources, so that different spatial resolutions do not affect the comparisons. Our estimate of source extension arises by comparing flux densities measured through the IRS slit with total flux densities of sources measured photometrically by IRAS. This is the criterion we have used to restrict our sample to unresolved sources, as now described.

We first examined the IRS archive of *Spitzer*, selecting sources having both IRS low resolution spectra and complete flux measures with IRAS. This yielded a sample of 501 sources. For these sources, we extracted all IRS LL1 spectra and determined the ratio of synthetic IRAS $25 \mu\text{m}$ flux density measured on the IRS spectrum, $f_\nu(\text{IRS } 25 \mu\text{m})$, compared to the $f_\nu(\text{IRAS } 25 \mu\text{m})$ observed with IRAS. Comparing the total $f_\nu(\text{IRAS } 25 \mu\text{m})$ with the $f_\nu(\text{IRS } 25 \mu\text{m})$ measured with the $10.7''$ slit of the IRS LL1 gives a measure of source extension. The resulting distribution is shown in Figure 2.

Figure 2 shows a concentration of sources near a value of $f_\nu(\text{IRAS } 25 \mu\text{m})/f_\nu(\text{IRS } 25 \mu\text{m})$ of unity, as expected for unresolved sources. There is a dispersion of $\sim 20\%$ for the core distribution near unity. This dispersion reflects uncertainties in the comparative flux calibrations of the IRS and IRAS and in the synthetic photometry, because real values below unity cannot occur (unless sources are actually variable).

To accommodate the dispersion arising from such uncertainties while minimizing uncertainties arising from aperture corrections for extended sources, we selected from the initial sample of 501 objects only those objects having flux ratios $f_\nu(\text{IRAS } 25 \mu\text{m})/f_\nu(\text{IRS } 25 \mu\text{m}) < 1.5$. This results in a final sample of 301 objects. This selection criterion assures that

²<http://isc.astro.cornell.edu/IRS/SmartDoc>

the final sample of 301 sources can be considered as spatially unresolved sources at infrared wavelengths longer than $\sim 20 \mu\text{m}$, so that the IRS spectral parameters refer to the same source as the longer wavelength SEDs from IRAS.

We do not apply corrections for slight source extension by using values of $f_\nu(\text{IRAS } 25 \mu\text{m})/f_\nu(\text{IRS } 25 \mu\text{m})$. This is partly because much of the differences from unity can be attributed to flux uncertainties. It is also because slightly resolved sources would not necessarily have the same spectra and SEDs throughout the source, so the true corrections are unknown. The resulting overall uncertainties in comparing IRS spectral parameters to IRAS and AKARI photometry are reflected in the empirical dispersions for these relations discussed in sections 3.2 and 3.4. All spectroscopic and photometric data for our final sample are listed in Tables 1-6.

The primary spectral parameter used in our analysis is at $\sim 8 \mu\text{m}$, which is observed with the IRS SL module, having a narrower slit ($3.7''$) compared to LL. In a few cases, sources are resolved at this scale, which is noted in a lack of overlap between the SL and LL portions of the spectrum. In such cases, the SL flux densities are increased by the factor needed to overlap LL (the "stitching" factor).

To measure total infrared luminosity for sources, we use L_{IR} defined as in Sanders and Mirabel (1996), with $f_{IR} = 1.8 \times 10^{-11}[13.48f_\nu(12) + 5.16f_\nu(25) + 2.58f_\nu(60) + f_\nu(100)]$, for f_{IR} in $\text{erg cm}^{-2} \text{s}^{-1}$ and IRAS flux densities $f_\nu(12)$, $f_\nu(25)$, $f_\nu(60)$, and $f_\nu(100)$ in Jy. This relation includes an estimate for additional long wavelength flux beyond the $100 \mu\text{m}$ limit of IRAS.

L_{IR} is a measure of total luminosity which is reradiated by absorbing dust. When sources are heavily obscured in all directions, L_{IR} is also a measure of bolometric luminosity, because primary radiation from all shorter wavelengths is always absorbed and reemitted from the dust. If absorption by dust is not uniform over all directions, as in AGN having increased absorption within a dusty torus, L_{IR} underestimates the true bolometric luminosity.

Our sample is representative of fainter, flux limited infrared samples chosen with IRAS or *Spitzer*. This is illustrated in Figure 3 by comparing mid infrared $f_\nu(25 \mu\text{m})$ with near infrared $f_\nu(1.2 \mu\text{m})$ from the Two Micron All Sky Survey (2MASS; Skrutskie et al. (2006)). This comparison shows the ratio of dust continuum to continuum from stars or non-thermal AGN continuum. Results indicate that the present sample spans the full range of dust obscuration and dust emission found in any sample of infrared-discovered sources brighter than 10 mJy at $25 \mu\text{m}$.

2.1. Infrared and Optical Spectral Classifications

We desire to relate the local objects in the present sample to spectroscopic classifications for dusty sources at $z \sim 2$. Our primary spectroscopic classification, therefore, is a classification of starburst, AGN, or composite (starburst plus AGN) derived from spectra at rest frame wavelengths between approximately $5 \mu\text{m}$ and $12 \mu\text{m}$ because these are the rest frame wavelengths observed with the IRS for $z \gtrsim 2$ (Figure 1).

The single most important parameter in these IRS spectra for a mid-infrared measure of the starburst component is the flux in PAH molecular emission features (Genzel et al. 1998; Brandl et al. 2006; Houck et al. 2007; Weedman and Houck 2009a; Sargsyan and Weedman 2009; Farrah et al. 2009b). The photodissociation region at the interface between the surrounding molecular cloud and the HII region of a starburst provides the appropriate physical conditions for strong PAH excitation and emission (Peeters et al. 2004). Our spectral classification for starbursts, AGN, and composites depends only on the strength of these PAH features.

Figure 4 shows the total infrared luminosity L_{IR} determined using IRAS fluxes compared with the rest-frame equivalent width of the $6.2 \mu\text{m}$ PAH feature for our sample of sources. The $\text{EW}(6.2 \mu\text{m})$ determines the fraction of starburst (SB) compared to AGN luminosity; the divisions into AGN, Composite and SB which we adopt are illustrated in Figure 4.

These divisions derive from previous studies with the IRS of sources having optical classifications. The definition of "pure starburst", with $\text{EW}(6.2 \mu\text{m}) > 0.4 \mu\text{m}$, arose originally from empirical measures of infrared spectra from the sample of optically classified starbursts in Brandl et al. (2006); this EW value was subsequently found to divide starbursts and AGN in infrared flux-limited samples (Weedman and Houck 2009a; Wu et al. 2010). Figure 4 shows the comprehensive range of our sample in both AGN/starburst fraction and in luminosity.

Perfect agreement between infrared and optical classifications is not expected for these dusty, obscured sources in which the primary luminosity source is often completely hidden optically. There are also well known examples of optical AGN with circumnuclear starbursts, so either might dominate the infrared spectrum. Figure 4 nevertheless shows the general consistency between infrared and optical classifications, using classifications derived from optical spectra with the Sloan Digital Sky Survey (SDSS; Gunn et al. (1998)) given in Tables 1, 3, and 5.

Sources are separated in these Tables according to the classifications of $\text{EW}(6.2 \mu\text{m})$ in Figure 4. For starbursts in Table 1, optical spectra when available show indications of an AGN in only one of 19 sources classified as starburst using the infrared criterion;

the one is a composite classification. Composite sources in Table 3 show a mix of optical classifications, as expected. Using the limited number of AGN in Table 5 which have optical spectral classifications, optical spectra when available show the presence of an AGN (AGN or composite optical classification) in 50 of 56 sources classified as AGN using the infrared criterion.

The spectral features at rest frame wavelengths $\sim 8 \mu\text{m}$ (Figure 1) which we use to make uniform measures of source luminosity can be traced with the IRS through all redshifts for $0 < z \lesssim 3$. For starbursts, the spectral peak is at $7.7 \mu\text{m}$ and arises from PAH emission; for absorbed AGN, this peak is not an emission feature but is a continuum maximum between absorption features and is typically at $7.9 \mu\text{m}$. In all of our measurements and discussion for this paper, we measure the spectral peak whenever such a peak is present, and we refer in general to such measurements of the peak as $f_\nu(\sim 8 \mu\text{m})$. For silicate emission AGN without either detectable PAH at $7.7 \mu\text{m}$ or a localized continuum maximum, our measures are of the continuum at $7.9 \mu\text{m}$, which we also define as $f_\nu(\sim 8 \mu\text{m})$.

Our measure of $\text{EW}(6.2 \mu\text{m})$ makes the assumption that this feature is a Gaussian on an underlying continuum which is the continuum immediately adjacent to the Gaussian, the standard definition of EW. We use this measure of EW to provide a consistent parameter among various sources, even those with poor S/N. In reality, the PAH features are broad and complex, and the $6.2 \mu\text{m}$ feature rests on wings of other PAH features, so that the adjacent continuum is not the true underlying continuum from dust emission. The complex of PAH features can be deconvolved if assumptions are made regarding relative fluxes and the spectral distribution of the underlying dust continuum (Smith et al. 2007). An accurate deconvolution is not feasible in the spectra of faint sources at high redshift which have poor S/N and limited spectral coverage; this is why we have introduced the peak $\nu f_\nu(7.7 \mu\text{m})$ as a measure of PAH luminosity.

To demonstrate that the peak $\nu f_\nu(7.7 \mu\text{m})$ is equivalent to measuring the total flux within an individual PAH feature for starbursts (and only starbursts), we compare in Figure 5 the $\nu f_\nu(\sim 8 \mu\text{m})$ for all sources with the total flux measured in the PAH $6.2 \mu\text{m}$ feature. For starbursts, most composites, and many AGN, $f_\nu(\sim 8 \mu\text{m})$ is the peak of the $7.7 \mu\text{m}$ PAH feature; for AGN and a few composites without a $7.7 \mu\text{m}$ PAH feature, $f_\nu(\sim 8 \mu\text{m})$ is the continuum at $7.9 \mu\text{m}$. Figure 5 shows, as expected, that weaker PAH measured by EW corresponds to an increased underlying dust continuum which artificially enhances the peak $\nu f_\nu(\sim 8 \mu\text{m})$. An increasing contribution to the dust continuum at $8 \mu\text{m}$ from an AGN which underlies the PAH feature from a starburst would explain all of the trends seen in this plot.

For the sources we classify as "pure" starbursts, with $\text{EW}(6.2 \mu\text{m}) > 0.4 \mu\text{m}$, the

median and 1σ dispersion in Figure 5 for the ratio $\nu f_\nu(7.7 \mu\text{m})/1000 f(6.2 \mu\text{m})$ is 0.065 ± 0.006 . This empirical result indicates a 10 % uncertainty in use of the peak $\nu f_\nu(7.7 \mu\text{m})$ to measure PAH luminosity from a starburst when compared to a measure of total luminosity in individual PAH features. This uncertainty is a measure of varying levels for the true dust continuum underlying the PAH features, but this is not an uncertainty in the luminosity of the starburst as measured by $\nu f_\nu(7.7 \mu\text{m})$ if the underlying continuum also arises from dust heated only by the starburst.

3. Discussion

3.1. Total Infrared Fluxes Compared to Spectral Parameters

Our previous summaries determined luminosities of dusty, obscured sources discovered with *Spitzer* using $\nu L_\nu(\sim 8 \mu\text{m})$, and showed that the most luminous starbursts and AGN show luminosity evolution in this parameter of form $(1+z)^{2.5}$ to $z \sim 2.5$ (Weedman and Houck 2008, 2009b). Transforming $\nu L_\nu(\sim 8 \mu\text{m})$ to L_{IR} is a crucial calibration for determining star formation rates (SFR) derived from total infrared luminosities as in Kennicutt (1998), and for measuring total luminosities of AGN. Our initial calibrations for sources to $z \sim 2.5$ were based on small samples and need improvement to determine how the calibrations depend on starburst/AGN fraction and on luminosity. Improving this calibration is the objective of this section.

Using sources classified in Tables 1, 3, and 5 as "pure" starbursts [$EW(6.2 \mu\text{m}) > 0.4 \mu\text{m}$], composite sources [$0.1 \mu\text{m} < EW(6.2 \mu\text{m}) < 0.4 \mu\text{m}$], and "pure" AGN [$EW(6.2 \mu\text{m}) < 0.1 \mu\text{m}$], we show in Figure 6 the ratios $f_{IR}/\nu f_\nu(\sim 8 \mu\text{m})$ for all sources. It is these ratios that allow estimates of total infrared luminosities L_{IR} when only mid-infrared spectra are available.

For starbursts in Figure 6, the median $\log [f_{IR}/\nu f_\nu(7.7 \mu\text{m})] = 0.74 \pm 0.18$. (A value of 0.78 was used in Weedman and Houck (2008).)

For most composite sources, the PAH features are sufficiently strong that the spectral peak is at $7.7 \mu\text{m}$, but for some sources with weak PAH and silicate absorption, the peak is at $7.9 \mu\text{m}$, as noted in Table 3. In Figure 6, the median $\log [f_{IR}/\nu f_\nu(7.7 \mu\text{m} \text{ or } 7.9 \mu\text{m})] = 0.96 \pm 0.26$. (Composite sources were not used in our previous analyses of "pure" starbursts or "pure" AGN.)

For AGN, there is sometimes a sufficiently strong $7.7 \mu\text{m}$ PAH feature that this is the spectral peak. The spectral peak is at $\sim 7.9 \mu\text{m}$ if the source has silicate absorption. If the

source has no localized peak near $8 \mu\text{m}$, either from PAH emission or silicate absorption, our spectral measurement is made at a wavelength of $7.9 \mu\text{m}$. Which parameter is measured is noted in Table 5. All AGN are combined in Figure 6 for comparison to starbursts and composite sources, but the $f_{IR}/\nu f_\nu(7.7 \mu\text{m}$ or $7.9 \mu\text{m})$ is determined separately for silicate absorption and silicate emission AGN as shown in Figure 7.

For silicate emission AGN in Figure 7, the median $\log [f_{IR}/\nu f_\nu(\sim 8 \mu\text{m})] = 0.51 \pm 0.21$. (A value of 0.74 was used in Weedman and Houck (2009b).)

For silicate absorption AGN in Figure 7, the median $\log [f_{IR}/\nu f_\nu(\sim 8 \mu\text{m})] = 0.80 \pm 0.25$. (A value of 0.95 was used in Weedman and Houck (2009b).) Although this is the median and dispersion for all absorbed AGN, Figure 7 indicates that the most strongly absorbed sources have systematically larger values of $f_{IR}/\nu f_\nu(\sim 8 \mu\text{m})$. This can be explained if the absorption also affects the continuum at $\sim 8 \mu\text{m}$, such that luminosity removed from the mid-infrared reappears in the far infrared. This is consistent with an extinction correction discussed more below.

That the largest values of $f_{IR}/\nu f_\nu(\sim 8 \mu\text{m})$ arise for composite sources is an interesting result from Figure 6. The composite sources are defined by intermediate strength of the PAH features. If composites are any combination of AGN and starbursts such as those included in the AGN and starburst samples, the composites should have $f_{IR}/\nu f_\nu(\sim 8 \mu\text{m})$ within the range of these ratios for AGN and starbursts. But the composite ratio exceeds both.

There is an explanation for the composite sources which can explain this result. This would arise if the "composite" classification includes sources with PAH which is weak because the PAH from the starbursts in these sources are more obscured compared to the PAH within the "starburst" classification. In this circumstance, the PAH would be weakened by absorption, and the absorbed luminosity would reappear at longer wavelengths. This would produce larger values of $f_{IR}/\nu f_\nu(\sim 8 \mu\text{m})$. Adopting this explanation implies that that sources with the greatest far-infrared luminosity and the coolest dust are sources at the extreme of obscuration for starbursts. This question is considered again in section 3.4 in context of SEDs.

3.2. Luminosities of the Most Luminous Starbursts and AGN

Using all available IRS observations, Weedman and Houck (2008, 2009b), and Houck and Weedman (2010) fit luminosity evolution for $0 < z < 2.5$ of the most luminous starbursts and absorbed AGN as measured by $\nu L_\nu(\sim 8 \mu\text{m})$. This is the parameter used in the present paper for comparison to L_{IR} , so that luminosity evolution in L_{IR} can be determined using the ratios

$f_{IR}/\nu f_\nu(\sim 8 \mu\text{m})$ determined above.

Using our new calibrations together with these forms of evolution, we can determine the total luminosity L_{IR} as a function of redshift for the most luminous dusty starbursts and AGN. Results are:

a) For the most luminous starbursts,

$$\log L_{IR}(\text{SB}) = 11.8 \pm 0.18 + 2.5(\pm 0.3) \log(1+z) \text{ for } L_{IR} \text{ in } L_\odot. \quad (1)$$

An important use of $L_{IR}(\text{SB})$ is to determine star formation rate (SFR) from the precepts of Kennicutt (1998), for which $\log(\text{SFR}) = \log L_{IR} - 9.76$, for SFR in units of $M_\odot \text{ yr}^{-1}$ and L_{IR} in L_\odot .

b) For the most luminous obscured, silicate absorption AGN,

$$\log L_{IR}(\text{AGN}_{\text{obscured}}) = 12.2 \pm 0.25 + 2.6(\pm 0.3) \log(1+z) \text{ for } L_{IR} \text{ in } L_\odot. \quad (2)$$

In the "unified model", the only difference between emission and absorption AGN is the viewing angle. Our results are consistent with this model such that all AGN have intrinsically similar total infrared luminosity, but absorbed AGN appear fainter in mid-infrared wavelengths because of absorption at those wavelengths. The absorbed luminosity from the mid-infrared spectrum reappears at longer wavelengths. We have found in section 3.1 that the median $f_{IR}/\nu f_\nu(\sim 8 \mu\text{m}) = 6.5$ for absorption sources and 3.2 for emission sources, as shown in Figure 7. This implies a factor of two extinction correction is required for $f_\nu(\sim 8 \mu\text{m})$ for the absorbed sources.

Because of insufficient sources in the various redshift bins, Weedman and Houck (2009b) did not fit the form of evolution for silicate emission sources. The luminosity distribution $\nu L_\nu(\sim 8 \mu\text{m})$ with redshift for silicate emission sources is updated in Houck and Weedman (2010). This distribution has similar shape to the distribution of absorbed sources, except that the emission sources are offset to brighter $\nu L_\nu(\sim 8 \mu\text{m})$ luminosities. This offset is consistent with the factor of two which would arise from the extinction correction for the absorbed sources. We conclude, therefore, that L_{IR} for the most luminous emission sources

is the same as for the most luminous absorbed sources. With this conclusion, the luminosity evolution for the most luminous unobscured, silicate emission, type 1 AGN also becomes:

$$\log L_{IR}(\text{AGN1}) = 12.2 \pm 0.21 + 2.6(\pm 0.3) \log(1+z) \text{ for } L_{IR} \text{ in } L_{\odot}. \quad (3)$$

These results are similar to those in Weedman and Houck (2009b) and Houck and Weedman (2010), but the $\log L_{IR}$ are systematically less luminous because of changes in the $f_{IR}/\nu f_{\nu}$ ($\sim 8 \mu\text{m}$) calibration. For starbursts, $\log L_{IR}(\text{SB})$ decreases by 0.04; for silicate absorption AGN, $\log L_{IR}(\text{AGN}_{obscured})$ decreases by 0.14; and for silicate emission AGN, $\log L_{IR}(\text{AGN1})$ decreases by 0.23 compared to our earlier conclusions.

These three equations indicate that, within uncertainties, the total infrared luminosities of the most luminous starbursts and most luminous AGN are similar to within a factor ~ 2 . This result is also consistent with observed spectra representing the brightest examples shown in Figure 1. The brightest sources observed at $z = 2.5$ in rest-frame f_{ν} ($\sim 8 \mu\text{m}$) scale as illustrated, with $f_{\nu}(7.9 \mu\text{m}, \text{AGN1}) : f_{\nu}(7.9 \mu\text{m}, \text{AGN}_{obscured}) : f_{\nu}(7.7 \mu\text{m}, \text{SB}) = 12 : 5 : 2$, in mJy. Applying our $f_{IR}/\nu f_{\nu}$ ($\sim 8 \mu\text{m}$) calibrations to these values of f_{ν} ($\sim 8 \mu\text{m}$) then yields $L_{IR}(\text{AGN1}) : L_{IR}(\text{AGN}_{obscured}) : L_{IR}(\text{SB}) = 3.5 : 2.9 : 1.0$ for these individual brightest examples. Scaling from the formal equations 1-3 would give the similar result that $L_{IR}(\text{AGN1}) : L_{IR}(\text{AGN}_{obscured}) : L_{IR}(\text{SB}) = 2.5 : 2.5 : 1.0$.

It is important to note, however, that $L_{IR}(\text{AGN})/L_{IR}(\text{SB})$ probably underestimates the value of this ratio for total bolometric luminosities. If AGN luminosity is absorbed only within an obscuring torus where absorbing dust produces $L_{IR}(\text{AGN})$, some primary radiation would escape the torus without being absorbed. This escaping radiation is not included in our measure of $L_{IR}(\text{AGN})$. By contrast, starbursts arising within the obscuring torus would have all of their bolometric luminosity absorbed and reradiated by the dust.

Our previous analyses which determined these forms of luminosity evolution were separated for sources classified as predominantly starbursts or predominantly AGN. This was done in an effort to determine if evolution appears different for these categories. The similarity of the results shows that luminosity evolution occurs together for starbursts and AGN as classes of sources. Whatever process triggers the formation of luminous, dusty galaxies triggers both starbursts and AGN. This conclusion does not, however, determine for an individual galaxy whether there is evolution between starburst and AGN. Descriptions of such "individual evolution" from one class to another (e.g. Sanders and Mirabel 1996;

Spoon et al. 2007; Farrah et al. 2009b) are consistent with the similarity of overall luminosity evolution which we find for both classes.

In our view, the most important question regarding individual evolution is whether AGN or starbursts came first in the early universe. We now have extensive samples of both to redshifts approaching 3, with no evidence of differences in evolution for these different classes of luminous infrared sources. Answering the crucial questions will require discovery and classification of luminous, dusty galaxies at higher redshifts.

3.3. Shapes of Spectral Energy Distributions

The *Spitzer* IRS results summarized above trace evolution of luminous, dusty galaxies to $z \sim 2.5$. To follow such sources beyond such redshifts requires new far-infrared, submillimeter, and millimeter observations. Redshifts may not be available for such sources, other than estimates of photometric redshifts based on SED shapes. In this section, we determine empirically the median SEDs and dispersions of the sources classified spectroscopically. Our objective is to understand if SEDs are sufficiently different that sources can be classified with long wavelength photometric observations using only the SEDs.

To extend SEDs to longer wavelengths than available from IRAS, we use AKARI fluxes to $160 \mu\text{m}$ when available³. The most important use of these AKARI results is to consider the coolest dust components, as discussed below and illustrated in Figure 13. We note that there seem to be systematic differences between IRAS and AKARI photometric results at the level of $\sim 10\%$. These differences are shown in Figure 8.

In Figure 8, we show the median results for all 190 objects from our total sample of 301 that have complete AKARI flux density measures. This figure shows that the median SED is not smooth between $60 \mu\text{m}$ and $100 \mu\text{m}$ where IRAS and AKARI measures overlap. Discontinuities are present at the $\sim 10\%$ level for flux densities between $60 \mu\text{m}$ and $100 \mu\text{m}$. These discontinuities will also appear in our median SEDs for different classifications (starbursts, composites, and AGN) discussed below. We do not believe that these are real discontinuities in the SEDs and conclude that these arise from photometric uncertainties. These uncertainties are small compared to the observed dispersions among SEDs, so we make no effort at reconciling these differences. Refinements can be made when new photometry is

³IRAS flux densities were obtained from the IRAS Faint Source Catalog at <http://vizier.u-strasbg.fr/viz-bin/VizieR-4>. AKARI flux densities are from the AKARI catalog at <http://darts.isas.jaxa.jp/astro/akari/cas/tools/search/crossid.html>.

available from the Herschel Observatory (Pilbratt et al. 2010; Griffin et al. 2010).

The distribution of SEDs for all starburst sources as determined from IRAS and AKARI flux densities, in the rest frame normalized to the peak $\nu f_\nu(7.7 \mu\text{m})$, is shown in Figure 9. Solid lines show medians at the various observing wavelengths, and error bars show one σ dispersions at medians of the various rest frame wavelengths observed by IRAS and AKARI. The distribution of SEDs for all composite sources as determined from IRAS and AKARI flux densities, in the rest frame normalized to the peak $\nu f_\nu(7.7 \mu\text{m}$ or $7.9 \mu\text{m})$, is shown in Figure 10, and the distribution of SEDs for all AGN is shown in Figure 11. The dispersions among the SEDs are compared in Figure 12. There are several notable results from these comparisons.

The "pure" starbursts show the most consistent spectra at all wavelengths. The dispersions generally range only over a factor of two at any wavelength. This means that a mid-infrared classification as starburst is a good predictor of far infrared properties.

As known since IRAS, typical SEDs for AGN are flatter than for starbursts, because AGNs contain a component of hotter dust that raises the mid-infrared dust continuum compared to the far infrared. This result is evident in Figure 12. When considering the dispersion among sources, however, the AGN are not invariably distinct from starbursts. The dispersions shown in Figure 12 overlap. There are many objects classified purely as AGN in the mid-infrared spectrum which have cool dust components as significant as in starbursts. As already commented above in section 3.1, the coolest dust components (greatest far infrared luminosities) are found in the composite sources, those with weak mid-infrared indicators of a starburst.

What is the source of the cool dust component in AGN and in the composite sources? In context of dusty torus models for AGN, it has been suggested that the cool dust is also heated by the AGN (e.g. Polletta et al. 2008) but is cool either because it is far from the AGN or is behind optically thick dust. A more common assumption is that cool dust is invariably a starburst indicator (e.g. Farrah et al. 2009b); in this case, the absence of starburst signatures in the mid-infrared for composite sources and AGN would be attributed to very heavy extinction of the starburst luminosity.

Despite this ambiguity in the far-infrared SEDs, Figures 9-11 illustrate that there are limits to the shape of SEDs, such that sources with spectra flatter than such limits are always "pure" AGN. This means that far infrared SEDs can define a sample of AGN, but it will not be a complete sample because of the many AGN with cool components. This is shown quantitatively in Figure 13 where the cool dust component as measured by $\nu f_\nu(160 \mu\text{m})/\nu f_\nu(18 \mu\text{m})$ from AKARI fluxes is compared with strength of the starburst as measured

by the PAH 6.2 μm feature.

The values of this ratio show how starbursts have systematically cooler dust than AGN. The median $\nu f_\nu(160 \mu\text{m})/\nu f_\nu(18 \mu\text{m})$ for starbursts is 1.74, for composites is 1.71, and for AGN is 0.47. These results indicate that the median "pure starburst" radiates almost 4 times more luminosity in the cool dust component relative to warm dust than does the median AGN. The dispersion of points shows that sources which are AGN dominated in the mid-infrared, as determined by the strength of PAH, can nevertheless have cool dust components. Pure starbursts cannot, however, have strong hot dust components, because the lower limit of this ratio for pure starbursts (0.7) is greater than the median for AGN (0.47).

The resulting quantitative conclusion is that any source with $\nu f_\nu(160 \mu\text{m})/\nu f_\nu(18 \mu\text{m}) < 0.7$ must have part of the bolometric luminosity arising from an AGN. Any source with $\nu f_\nu(160 \mu\text{m})/\nu f_\nu(18 \mu\text{m}) < 0.5$ can confidently be classified as having dust continuum luminosity at all wavelengths arising primarily from an AGN, with negligible starburst contribution.

3.4. Averages and Dispersions for Spectra

The preceding results illustrate the dispersions in overall SEDs among the sources in the sample. It is also useful to illustrate averages and dispersions within the IRS spectra. Dispersions among spectra of different classifications are shown in Figure 14. This result for the spectral dispersions is similar to the result discussed above for the photometric SEDs. The largest dispersions are among the composite sources and absorbed AGN, noticeably larger than for pure starbursts.

As emphasized in the Introduction, much of our motive for this study is to make comparisons between the local sources in this sample and the numerous sources at $z \gtrsim 2$ which have been discovered with *Spitzer* IRS spectroscopy. To facilitate such comparisons, we show in Figure 15 the average spectra of sources with different classifications, as they would appear in the observed frame if redshifted to $z = 2.5$. Only those portions of the spectrum with $\lambda \lesssim 35 \mu\text{m}$ are visible in IRS spectra; similarities in this wavelength range with the examples in Figure 1 are evident.

4. Summary and Conclusions

Spectroscopic results with the *Spitzer* Infrared Spectrograph are compared to photometric SEDs to 160 μm from IRAS and AKARI for 301 sources. Sources are selected to be spatially unresolved by comparing spectroscopic and photometric flux densities at 25 μm , so that spectra and SEDs can be reliably compared. Sources have $0.004 < z < 0.34$ and $42.5 < \log L_{IR} < 46.8$ (erg s^{-1}) and cover the full range of starburst galaxy and AGN classifications. All spectra are newly determined with an optimal extraction procedure and made available electronically (<http://cassis.astro.cornell.edu/sargsyan-et-al>).

A consistent spectroscopic classification is used for sources and compared to optical classifications. The infrared classification derives from EW of the 6.2 μm PAH emission, defining starbursts [$\text{EW}(6.2 \mu\text{m}) > 0.4 \mu\text{m}$], composite sources [$0.1 \mu\text{m} < \text{EW}(6.2 \mu\text{m}) < 0.4 \mu\text{m}$], and AGN [$\text{EW}(6.2 \mu\text{m}) < 0.1 \mu\text{m}$].

Total infrared luminosities L_{IR} and SEDs are compared to the 7.7 μm PAH spectral peak for sources with PAH features or to the dust continuum at 7.9 μm for AGN without PAH features. We find that $\log [L_{IR}/\nu L_{\nu}(7.7 \mu\text{m})] = 0.74 \pm 0.18$ in starbursts, that $\log [L_{IR}/\nu L_{\nu}(7.7 \mu\text{m})] = 0.96 \pm 0.26$ in composite sources (starburst plus AGN), that $\log [L_{IR}/\nu L_{\nu}(7.9 \mu\text{m})] = 0.80 \pm 0.25$ in AGN with silicate absorption, and $\log [L_{IR}/\nu L_{\nu}(7.9 \mu\text{m})] = 0.51 \pm 0.21$ in AGN with silicate emission. There is no dependence of these ratios on L_{IR} .

These scaling ratios are used to determine L_{IR} from IRS spectra for the most luminous sources yet discovered (at $z \sim 2.5$). It is found that L_{IR} are similar for the most luminous silicate absorption and silicate emission AGN, and the L_{IR} for the most luminous AGN are about 2.5 times larger than for the most luminous starbursts.

Starbursts show the most consistent spectra and SEDs at all wavelengths. The dispersions generally range only over a factor of two at any wavelength. This means that a mid-infrared classification as starburst is a good predictor of far infrared properties. Sources with the strongest far infrared luminosity from cool dust components are composite sources, indicating that these sources may contain the most obscured starbursts. Typical SEDs for AGN are flatter than for starbursts, but many objects classified as AGN in the mid-infrared spectrum have cool dust components as significant as in starbursts.

Comparison of SEDs indicates that any source with $\nu f_{\nu}(160 \mu\text{m})/\nu f_{\nu}(18 \mu\text{m}) < 0.7$ must have part of the bolometric luminosity arising from an AGN. Any source with $\nu f_{\nu}(160 \mu\text{m})/\nu f_{\nu}(18 \mu\text{m}) < 0.5$ can confidently be classified as having dust continuum luminosity at all wavelengths arising primarily from an AGN, with negligible starburst contribution.

This work is based primarily on observations made with the Spitzer Space Telescope, which is operated by the Jet Propulsion Laboratory, California Institute of Technology, under NASA contract 1407. This work made use of the NASA/IPAC Extragalactic Data Base (NED) operated by JPL/Caltech under contract with NASA. Support for this work by the IRS GTO team at Cornell University was provided by NASA through Contract Number 1257184 issued by JPL/Caltech.

REFERENCES

- Armus, L. et al. 2007, *ApJ*, 656, 148
- Bouwens, R. J. et al. 2009, *ApJ*, 705, 936
- Brand, K. et al. 2008a, *ApJ*, 673, 119
- Brand, K. et al. 2008b, *ApJ*, 680, 119
- Brandl, B. et al. 2006, *ApJ*, 653, 1129.
- Calzetti, D. 2008, *Astronomical Society of the Pacific Conference Series*, 390, 121
- Chapman, S. C. et al. 2010, *MNRAS*, 409, L13
- Dasyra, K. M. et al. 2009, *ApJ*, 701, 1123
- Desai, V. et al. 2009, *ApJ*, 700, 1190
- Farrah, D. et al. 2007, *ApJ*, 667, 149
- Farrah, D. et al. 2008, *ApJ*, 677, 957
- Farrah, D., Weedman, D., Lonsdale, C.J., Polletta, M., Rowan-Robinson, M., Houck, J., and Smith, H.E. 2009, *ApJ*, 696, 2044
- Farrah, D. et al. 2009b, *ApJ*, 700, 395
- Genzel, R. et al. 1998, *ApJ*, 498, 579
- Gunn, J. E., et al. 1998, *AJ*, 116, 3040
- Griffin, M. et al. 2010, *A&A*, 518, 3
- Hao, L. et al. 2005, *ApJ*, 625, L75

- Hernan-Caballero, A. et al. 2009, MNRAS, 395, 1695
- Higdon, S.J.U. et al. 2004, PASP, 116, 975
- Houck, J. R. et al. 2004, ApJS, 154, 18
- Houck, J.R. et al. 2005, ApJ, 622, L105
- Houck, J. R., Weedman, D.W., LeFloc'h, E., and Hao, L. 2007, ApJ, 671, 323
- Houck, J.R, and Weedman, D.W, 2010, in press, "Reionization to Exoplanets: *Spitzer's* Growing Legacy", ASP Conference Series, ed: P. Ogle, arXiv1005.0344H
- Hovhannisyian, A., Sargsyan, L. A., Mickaelian, A. M., and Weedman, D. W., Astrofizika, in press
- Huang, J. S. et al. 2009, ApJ, 700, 183
- Hunt, L. K, Thuan, T. X., Izotov, Y. I., and Sauvage, M. 2010, ApJ, 712, 164.
- Imanishi, M., Dudley, C. C., Maiolino, R., Maloney, P. R., Nakagawa, T., and Risaliti, G. 2007, ApJ, 171, 72
- Kaneda, H., Kim, W., Onaka, T., Wada, T., Ita, Y., Sakon, I., and Takagi, T. 2007, PASJ, 59, S423
- Kawada, M., et al. 2007, PASJ, 59, S389
- Kennicutt, R.C. 1998, ARA&A, 36, 18
- Lebouteiller, V., Bernard-Salas, H., Sloan, G. C., and Barry, D. J. 2010, PASP, 122, 231
- Madau, P., Pozzetti, L., and Dickinson, M. 1998, ApJ, 498, 106
- Markwick-Kemper, F., Gallagher, S. C., Hines, D. C., and Bouwman, J. 2007, ApJ, 668, L107
- Martinez-Sansigre, A., Lacy, M., Sajina, A., and Rawlings, S. 2008, ApJ, 674, 676
- Menendez-Delmestre, K. et al. 2009, ApJ, 699, 667
- Murakami, H., et al. 2007, PASJ, 59, S369
- Oliver, S. et al. 2010, A&A, 518, L21
- Onaka, T., et al. 2007, PASJ, 59, S401

- Peeters, E., Spoon, H.W.W., and Tielens, A.G.G.M. 2004, *ApJ*, 613, 986
- Pilbratt, G. et al. 2010, *A&A*, 518, 1
- Polletta, M., Weedman, D., Honig, S., Lonsdale, C. J., Smith, H. E., and Houck, J. 2008, *ApJ*, 675, 960
- Pope, A. et al., 2008, *ApJ*, 575, 1171
- Rowan-Robinson, M. et al. 2010, *MNRAS*, 409, L2
- Reddy, N. A. and Steidel, C. C. 2009, *ApJ*, 692, 778
- Rieke, G.H. et al., 2004, *ApJS*, 154, 25
- Sajina, A., Yan, L., Armus, L., Choi, P., Fadda, D., Helou, G., and Spoon, H. 2007, *ApJ*, 664, 713
- Sanders, D. B., and Mirabel, I. F. 1996, *ARA&A*, 34, 749
- Sargsyan, L., Mickaelian, A., Weedman, D., and Houck, J. 2008, *ApJ*, 683, 114
- Sargsyan, L. A. and Weedman, D. W. 2009, *ApJ*, 701, 139
- Sargsyan, L. A., Weedman, D. W., and Houck, J. R. 2010, *ApJ*, 715, 986
- Schweitzer, M. et al. 2008, *ApJ*, 679, 101.
- Shi, Y. et al. 2006, *ApJ*, 653, 127
- Skrutskie, M. F. et al. 2006, *AJ*, 131, 1163
- Smith, J. D. T. et al. 2007, *ApJ*, 656, 770
- Soifer, B. T., Neugebauer, G., and Houck, J. R. 1987, *ARA&A*, 25, 187
- Spoon, H. W. W. et al. 2007, *ApJ*, 654, L49
- Weedman, D.W., Le Floch, E., Higdon, S.J.U., Higdon, J.L., and Houck, J.R. 2006a, *ApJ*, 638, 613
- Weedman, D.W. et al. 2006b, *ApJ*, 653, 101.
- Weedman, D.W. and Houck, J.R. 2008, *ApJ*, 686, 127
- Weedman, D.W. and Houck, J.R. 2009a, *ApJ*, 693, 370

Weedman, D.W. and Houck, J.R. 2009b, ApJ, 698, 1682

Wright, E. L. 2006, PASP, 118, 1711

Wu, Y. et al. 2010, ApJ, 723, 895

Yan, L. et al. 2007, ApJ, 658, 778

Table 1. Spectroscopic Properties of Starbursts

source	Name	FSC Name	J2000 coordinates	z ^a	SDSS ^b	EW(6.2 μm) ^c μm	f(6.2 μm) ^d	f(11.3 μm) ^e	f_{ν} (7.7 μm) mJy
1	Mrk938	F00085-1223	001106.50-120626.0	0.0196	...	0.44	33.50	22.10	475.0
2	MCG-02-01-051	F00163-1039	001850.90-102236.7	0.0271	sb	0.56	24.40	17.24	389.4
3	IRAS00456-2904	F00456-2904	004806.75-284818.6	0.1103	...	0.43	3.06	2.26	56.9
4	MCG+12-02-001	F00506+7248	005403.88+730505.9	0.0157	...	0.53	49.90	33.67	810.1
5	MCG-03-04-014	F01076-1707	011008.93-165109.9	0.0335	...	0.45	25.26	24.39	513.8
6	ESO244-G012	F01159-4443	011808.31-442743.4	0.0229	...	0.54	34.15	23.78	555.9
7	ESO353-G020	F01325-3623	013451.26-360814.4	0.0159	...	0.40	31.51	23.40	634.0
8	UGC01385	F01519+3640	015453.82+365504.3	0.0188	...	0.54	18.90	15.87	294.2
9	IRASF02071-1023	F02071-1023	020938.52-100846.0	0.0128	...	0.66	62.19	44.42	854.9
10	UGC01845	F02208+4744	022407.97+475811.9	0.0156	...	0.44	41.24	33.50	772.7
11	UGC02238	F02435+1253	024617.46+130544.6	0.0219	...	0.46	34.00	22.07	718.1
12	UGC02369	F02512+1446	025401.84+145815.7	0.0312	...	0.43	15.59	10.44	262.3
13	IRASF03217+4022	F03217+4022	032505.37+403332.2	0.0234	...	0.41	14.43	11.75	259.3
14	MCG-05-12-006	F04502-3304	045204.96-325926.0	0.0188	...	0.40	14.80	14.69	263.0
15	NGC1808	F05059-3734	050742.32-373045.7	0.0033	...	0.58	283.00	229.22	4322.4
16	VIIZw031	F05081+7936	051646.39+794012.9	0.0537	...	0.49	22.08	18.13	397.3
17	IRASF05187-1017	F05187-1017	052106.53-101446.2	0.0283	...	0.41	6.03	3.88	104.9
18	UGC3608	F06538+4628	065734.41+462410.6	0.0187 ^a	...	0.42	9.55	7.87	168.5
19	IRASF06592-6313	F06592-6313	065940.26-631752.4	0.0230	...	0.40	10.98	10.49	199.0
20	IRASF08076+3658	F08076+3658	081056.13+364945.0	0.0215	sb	0.52	2.94	3.15	56.1
21	IRASF09168+3308	F09168+3308	091954.54+325559.0	0.0499	sb	0.49	6.96	5.12	119.7
22	IRASF09406+1018	F09406+1018	094321.62+100501.0	0.0538	sb	0.51	6.17	4.38	103.2
23	IRASF09471+3158	F09471+3158	095004.02+314442.0	0.0162	em+abs	0.56	6.14	5.27	96.8
24	Mrk25	F10003+5940	100351.90+592610.0	0.0100	sb	0.46	3.71	4.22	73.0
25	NGC3125	F10042-2941	100633.33-295606.6	0.0037	...	0.47	5.12	3.98	69.8
26	IRASF10332+6338	F10332+6338	103636.12+632222.0	0.0381	sb	0.52	3.22	2.39	52.6
27	UM448	F11396+0036	114212.30+002003.0	0.0186	sb	0.45	9.64	8.63	166.0
28	IRASF12020+5314	F12020+5314	120437.98+525717.0	0.0816	sb	0.48	1.97	1.39	32.4
29	Mrk206	F12220+6742	122417.00+672624.0	0.0044	sb	0.50	3.98	3.23	58.3
30	IRASF12538+6352	F12538+6352	125554.00+633644.0	0.0092	em+abs	0.58	16.54	6.61	241.0
31	CGCG043-099	F12592+0436	130150.28+042000.8	0.0375	...	0.44	15.34	8.21	285.8
32	IRASF13007+6405	F13007+6405	130239.21+634929.0	0.0416	sb	0.46	1.24	1.02	20.3
33	ESO507-G070	F13001-2339	130252.42-235517.8	0.0217	...	0.42	15.66	7.40	299.0
34	UGC08387	F13182+3424	132035.37+340822.2	0.0233	sb	0.46	31.14	15.89	592.7

Table 1—Continued

source	Name	FSC Name	J2000 coordinates	z ^a	SDSS ^b	EW(6.2 μm) ^c μm	f(6.2 μm) ^d	f(11.3 μm) ^e	$f_\nu(7.7 \mu\text{m})$ mJy
35	IRAS13539+2920	F13539+2920	135609.99+290535.0	0.1085	sb	0.42	3.30	2.01	63.0
36	IRAS14060+2919	F14060+2919	140819.09+290447.2	0.1168	sb	0.51	3.84	2.70	67.6
37	CGCG247-020	F14179+4927	141943.27+491411.9	0.0257	comp	0.45	14.66	12.59	253.8
38	IRASF15105+4727	F15105+4727	151212.86+471630.0	0.0535	sb	0.29	0.81	0.54	13.9
39	IRASF15545+4000	F15545+4000	155616.04+395137.0	0.0712	sb	0.51	3.19	2.75	53.1
40	IRAS16164-0746	F16164-0746	161911.75-075403.0	0.0272	...	0.44	17.87	9.68	338.2
41	CGCG052-037	F16284+0411	163056.53+040458.7	0.0245	...	0.51	23.15	17.86	395.1
42	ESO069-IG006	F16330-6820	163811.85-682608.2	0.0464	...	0.50	29.55	20.37	549.6
43	IRASF16474+3430	F16474+3430	164914.20+342510.1	0.1115	...	0.42	4.90	3.03	88.3
44	IRAS16569+8105	F16568+8104	165236.82+810016.6	0.0492	...	0.60	7.97	6.48	124.6
45	IRASF17132+5313	F17132+5313	171420.45+531031.6	0.0509	...	0.42	8.83	8.12	166.3
46	IRASF18293-3413	F18293-3413	183241.10-341127.0	0.0182	...	0.45	100.98	79.50	2077.5
47	ESO593-IG008	F19115-2124	191431.15-211906.3	0.0487	...	0.40	11.53	9.17	268.5
48	ESO286-G035	F21008-4347	210411.11-433536.1	0.0174	...	0.50	31.04	25.36	584.1
49	MCG-01-60-022	F23394-0353	234200.91-033654.4	0.0232	...	0.50	16.39	11.93	279.6
50	CGCG381-051	F23461+0157	234841.70+021423.0	0.0307	...	0.54	5.07	4.04	85.0
51	Mrk331	F23488+2018	235126.80+203510.0	0.0185	...	0.55	54.67	42.44	833.1

^aRedshift from optical redshift in NASA/IPAC Extragalactic Data Base (NED), except source 18, from IRS spectrum.

^bOur optical classification determined from spectra of the Sloan Digital Sky Survey, determined from presence of broad hydrogen emission lines or ratios among [OIII] λ 5007, H β , [NII] λ 6584, and H α .

^cRest frame equivalent width of 6.2 μm PAH feature fit with single gaussian on a linear continuum within rest wavelength range 5.5 μm to 6.9 μm .

^dTotal flux of PAH 6.2 μm feature fit with single gaussian on a linear continuum within rest wavelength range 5.5 μm to 6.9 μm in units of 10^{-20}W cm^{-2} .

^eTotal flux of PAH 11.3 μm feature fit with single gaussian on a linear continuum within rest wavelength range 10.5 μm to 12.0 μm in units of 10^{-20}W cm^{-2} .

Table 2. SEDs and Total Luminosities of Starbursts

source	FSC Name	$f_{\nu}(25)$ IRS Jy	$f_{\nu}(8)^a$ Jy	$f_{\nu}(12)^b$ Jy	$f_{\nu}(18)^a$ Jy	$f_{\nu}(25)^b$ Jy	$f_{\nu}(60)^b$ Jy	$f_{\nu}(65)^a$ Jy	$f_{\nu}(90)^a$ Jy	$f_{\nu}(100)^b$ Jy	$f_{\nu}(140)^a$ Jy	$f_{\nu}(160)^a$ Jy	$f_{\nu}(1.25)^c$ mJy	$f_{\nu}(1.66)^c$ mJy	R ^d	L_{ir}^e log
1	F00085-1223	1.563	0.269	0.350	...	2.390	17.050	14.430	17.041	16.860	12.127	11.149	18.97	29.61	7.73	45.07
2	F00163-1039	0.997	0.178	0.270	0.517	1.130	6.880	5.918	8.251	9.620	7.303	6.951	4.49	6.38	4.49	45.03
3	F00456-2904	0.161	...	0.084	...	0.141	2.600	2.557	2.479	3.380	4.084	...	1.41	1.78	10.77	45.79
4	F00506+7248	2.561	0.493	0.765	1.668	3.720	22.400	15.707	26.171	26.700	19.092	19.151	7.73	11.61	6.60	45.04
5	F01076-1707	0.737	0.203	0.301	0.511	0.846	6.480	5.944	8.097	10.400	10.367	5.217	8.52	14.98	3.30	45.20
6	F01159-4443	1.585	0.256	0.303	0.805	1.860	7.840	7.184	10.033	11.700	8.497	6.698	12.38	17.60	3.88	44.97
7	F01325-3623	0.550	0.226	0.258	0.341	0.677	7.290	7.159	11.084	15.800	16.619	13.424	10.3	17.73	3.08	44.61
8	F01519+3640	0.861	0.151	0.211	0.430	0.962	5.490	5.118	5.705	7.780	6.296	4.514	13.16	17.88	4.76	44.61
9	F02071-1023	1.245	0.514	0.537	0.861	1.790	9.230	10.695	12.442	20.800	12.052	9.280	12.27	19.57	3.34	44.59
10	F02208+4744	0.883	0.269	0.362	0.476	0.987	9.920	10.359	13.095	13.500	15.055	11.143	16.72	31.64	2.98	44.67
11	F02435+1253	0.436	0.382	0.403	0.333	0.565	7.700	7.658	12.144	15.300	16.353	13.074	6.85	11.66	2.86	44.91
12	F02512+1446	1.131	0.159	0.205	0.564	1.330	8.140	7.669	8.913	10.300	10.410	7.188	5.24	5.76	7.43	45.20
13	F03217+4022	0.699	0.198	0.205	0.398	0.852	7.160	7.327	8.674	10.400	9.984	7.070	7.63	11.65	6.57	44.89
14	F04502-3304	1.101	0.141	0.203	0.490	1.180	8.390	6.988	7.774	9.400	6.754	7.735	10.05	13.92	7.14	44.74
15	F05059-3734	10.858	3.538	4.430	7.591	16.100	87.80	124.12	115.25	137.00	98.83	114.42	62.07	82.55	3.23	44.33
16	F05081+7936	0.531	0.168	0.245	0.300	0.579	5.580	5.576	6.239	9.620	8.574	7.770	7.29	10.56	3.71	45.55
17	F05187-1017	0.196	...	0.059	...	0.180	4.960	5.048	6.636	8.100	6.607	6.302	3.06	5.18	10.25	44.85
18	F06538+4628	0.903	0.204	0.291	0.518	1.210	8.030	7.050	9.066	10.900	11.390	8.578	4.69	6.07	11.67	44.76
19	F06592-6313	0.736	0.101	0.155	0.402	0.797	5.740	5.047	5.649	7.560	5.785	3.980	9.66	13.69	6.79	44.77
20	F08076+3658	0.116	...	0.101	...	0.155	1.140	0.929	1.179	1.350	2.605	0.377	3.87	2.69	5.43	44.07
21	F09168+3308	0.226	...	0.100	...	0.320	2.630	4.140	3.42	4.51	5.64	45.14
22	F09406+1018	0.197	...	0.119	...	0.227	2.420	3.830	1.62	2.16	6.06	45.18
23	F09471+3158	0.167	...	0.099	...	0.219	1.180	1.184	1.160	1.380	1.934	1.290	8.66	...	3.34	43.85
24	F10003+5940	0.227	...	0.094	...	0.251	1.250	0.810	1.093	1.590	2.303	0.672	6.76	9.08	4.72	43.46
25	F10042-2941	0.513	...	0.200	0.443	0.791	5.040	3.617	5.193	5.130	5.715	5.136	2.9	2.75	16.55	43.12
26	F10332+6338	0.184	...	0.081	...	0.214	0.737	1.384	0.559	0.845	0.536	1.070	1.85	2.57	4.51	44.46
27	F11396+0036	0.568	0.090	0.140	0.378	0.715	4.140	3.191	4.557	4.320	3.867	5.044	5.76	12.81	5.83	44.44
28	F12020+5314	0.069	...	0.115	...	0.100	1.140	1.153	1.118	1.980	1.962	0.776	1.11	1.66	10.77	45.29
29	F12220+6742	0.232	...	0.085	0.131	0.221	1.190	0.766	0.967	1.640	...	1.056	3.31	3.68	5.57	42.72
30	F12538+6352	0.256	0.095	0.106	0.151	0.280	3.060	2.836	3.239	5.760	4.726	3.324	7	11.78	3.20	43.73
31	F12592+0436	0.352	0.107	0.156	0.322	0.386	5.070	4.881	5.809	7.950	7.178	6.005	4.72	7.79	4.21	45.15
32	F13007+6405	0.094	...	0.103	...	0.142	0.348	0.812	1.43	1.75	9.08	44.42
33	F13001-2339	0.763	...	0.137	0.330	0.846	13.700	12.938	13.232	15.300	15.519	9.197	3.95	6.38	8.98	45.02
34	F13182+3424	1.163	0.213	0.263	0.554	1.360	15.400	16.622	20.602	25.200	17.802	17.068	4.99	8.70	6.02	45.21

Table 2—Continued

source	FSC Name	$f_\nu(25)$ IRS Jy	$f_\nu(8)$ ^a Jy	$f_\nu(12)$ ^b Jy	$f_\nu(18)$ ^a Jy	$f_\nu(25)$ ^b Jy	$f_\nu(60)$ ^b Jy	$f_\nu(65)$ ^a Jy	$f_\nu(90)$ ^a Jy	$f_\nu(100)$ ^b Jy	$f_\nu(140)$ ^a Jy	$f_\nu(160)$ ^a Jy	$f_\nu(1.25)$ ^c mJy	$f_\nu(1.66)$ ^c mJy	R ^d	L_{ir} ^e log
35	F13539+2920	0.108	...	0.087	...	0.122	1.830	1.703	1.777	2.730	2.719	0.260	1.13	1.61	7.52	45.67
36	F14060+2919	0.159	...	0.096	...	0.144	1.610	1.349	1.495	2.420	1.653	1.869	1.11	1.54	6.57	45.70
37	F14179+4927	0.808	0.088	0.154	0.395	0.839	5.620	5.708	6.033	8.000	6.492	6.486	8.21	11.71	5.40	44.88
38	F15105+4727	0.109	...	0.102	...	0.116	0.384	0.662	0.63	1.05	12.70	44.62
39	F15545+4000	0.160	...	0.097	...	0.159	0.791	1.133	0.625	0.937	1.412	0.434	2.05	2.67	4.76	45.03
40	F16164-0746	0.584	0.136	0.350	0.284	0.562	10.200	10.727	12.130	13.700	14.314	13.012	2.61	5.01	6.68	45.14
41	F16284+0411	0.718	0.208	0.291	0.414	0.770	6.950	7.249	8.012	12.100	10.881	6.101	8.09	12.13	4.54	44.95
42	F16330-6820	0.603	0.184	0.225	...	0.657	7.300	7.780	9.382	12.000	9.863	10.272	4.96	9.05	3.28	45.51
43	F16474+3430	0.166	...	0.126	...	0.205	2.270	2.279	2.235	2.880	2.690	1.959	1.47	2.20	6.68	45.79
44	F16568+8104	0.138	...	0.091	...	0.167	1.560	1.769	1.665	3.730	2.959	2.214	3.53	5.27	3.83	44.98
45	F17132+5313	0.428	0.127	0.122	0.299	0.620	5.680	5.354	5.937	8.040	6.699	5.258	5	8.38	8.04	45.46
46	F18293-3413	3.121	...	1.120	...	3.760	34.20	36.66	35.20	49.70	35.21	45.24	17.77	31.76	3.90	45.35
47	F19115-2124	0.412	...	0.171	0.265	0.475	6.160	5.733	8.245	9.720	12.361	6.011	5.9	7.96	5.48	45.46
48	F21008-4347	0.613	0.252	0.294	0.368	0.775	6.930	7.103	9.880	12.600	11.441	9.431	12.07	7.79	3.09	44.66
49	F23394-0353	0.508	0.144	0.219	0.355	0.639	5.150	4.657	6.625	8.020	6.558	5.081	5.12	8.54	4.06	44.76
50	F23461+0157	0.325	0.088	0.510	0.301	0.180	1.750	1.643	1.684	2.760	2.651	1.863	2.18	3.10	8.45	44.75
51	F23488+2018	2.026	0.346	0.497	1.003	2.500	18.600	16.246	19.342	21.600	15.868	8.884	22.43	29.45	5.04	45.08

^aFlux densities at listed wavelengths taken from AKARI catalog, <http://darts.isas.jaxa.jp/astro/akari/cas/tools/search/crossid.html>.

^bFlux densities at listed wavelengths taken from IRAS Faint Source Catalog, <http://vizier.u-strasbg.fr/viz-bin/VizieR-4>.

^cFlux densities at listed wavelengths taken from 2MASS catalog.

^dRatio $R = f_{IR}/\nu f_\nu(7.7 \mu\text{m})$, for $f_{IR} = 1.8 \times 10^{-11}[13.48f_\nu(12) + 5.16f_\nu(25) + 2.58f_\nu(60) + f_\nu(100)]$ in $\text{erg cm}^{-2} \text{s}^{-1}$.

^eTotal infrared luminosity $L_{ir} = 4\pi D^2 f_{IR}$ in erg s^{-1} for D the luminosity distance determined for $H_0 = 71 \text{ km s}^{-1} \text{Mpc}^{-1}$, $\Omega_M=0.27$ and $\Omega_\Lambda=0.73$, from Wright (2006): <http://www.astro.ucla.edu/~wright/CosmoCalc.html>.

Table 3. Spectroscopic Properties of Composite Sources

source	Name	FSC Name	J2000 coordinates	z ^a	SDSS ^b	EW(6.2 μm) ^c μm	f(6.2 μm) ^d	f(11.3 μm) ^e	f_ν (7.7 μm) mJy
1	Mrk334	F00006+2141	000309.62+215736.6	0.0219	...	0.25	17.31	12.15	334.6
2	IRAS00199-7426	F00199-7426	002207.01-740941.7	0.0964	...	0.35	5.54	3.83	113.2
3	E12-G21	F00392-7930	004046.10-791424.0	0.0300	...	0.28	10.90	7.53	168.8
4	NGC0291	F00509-0902	005329.92-084604.1	0.0190	agn	0.33	5.17	4.97	111.4
5	CGCG436-030	F01173+1405	012002.63+142142.3	0.0312	sb	0.23	15.06	9.15	361.0
6	IRASF01197+0044	F01197+0044	012218.13+010026.0	0.0555	sb	0.14	3.23	1.86	83.7
7	IRASF01364-1042	F01364-1042	013852.91-102711.0	0.0482	agn	0.31	2.82	1.48	66.6
8	IIIZw035	F01417+1651	014430.56+170609.0	0.0274	...	0.37	4.48	4.93	106.8
9	IRAS02411-0353N	F02411+0353	024346.09+040636.9	0.1436	...	0.35	3.24	2.36	68.7
10	IRASF02417-0857	F02417-0857	024414.57-084420.9	0.0553	sb	0.19	1.29	0.90	35.8
11	IRASF02437+2122	F02437+2122	024639.13+213510.4	0.0233	...	0.15	4.14	3.91	127.1
12	Mrk1066	F02568+3637	025958.59+364914.3	0.0120	...	0.25	24.66	26.80	498.5
13	Mrk609	F03229-0619	032525.34-060838.7	0.0345	agn	0.32	9.76	11.11	192.8
14	IRASF03359+1523	F03359+1523	033847.07+153254.1	0.0354	...	0.36	4.05	5.05	104.2
15	ESO549-G049	F04001-1811	040225.66-180251.4	0.0263	...	0.23	7.95	8.77	167.7
16	NGC1510	F04018-4332	040332.60-432400.0	0.0030	...	0.38	1.25	1.24	18.7
17	IRAS04103-2838	F04103-2838	041219.53-283024.4	0.1175	...	0.18	2.64	2.19	71.9
18	IRAS04114-5117	F04113-5117	041244.92-510934.2	0.1246	...	0.34	1.63	1.13	36.0
19	ESO420-G013	F04118-3207	041349.70-320025.3	0.0119	...	0.21	30.58	28.76	708.7
20	IRASF06076-2139	F06076-2139	060945.74-214024.5	0.0374	...	0.24	4.78	3.61	121.0
21	IRAS06301-7934	F06301-7934	062642.20-793630.4	0.1564	...	0.15	0.55	0.39	23.1
22	NGC2273	F06456+6054	065008.72+605045.0	0.0061	...	0.13	17.97	19.71	493.4
23	Mrk622	F08043+3909	080741.04+390015.2	0.0232	comp	0.24	2.38	3.59	47.3
24	IRASF08273+5543	F08273+5543	083109.29+553316.0	0.0447	em+abs	0.30	0.90	0.77	17.0
25	IRASF08344+5105	F08344+5105	083803.63+505509.0	0.0967	sb	0.37	2.77	1.60	57.6
26	Mrk18	F08580+6020	090158.39+600906.0	0.0111	sb	0.27	7.96	8.22	145.4
27	IRASF10388+4033	F10388+4033	104148.04+401721.0	0.0692	comp	0.32	1.03	0.81	22.1
28	IRASF10398+1455	F10398+1455	104233.32+143954.0	0.0992	sb	0.31	1.82	1.92	34.9
29	NGC3367	F10439+1400	104634.96+134502.8	0.0101	comp	0.24	3.63	4.23	67.9
30	IRAS10494+4424	F10494+4424	105223.59+440846.5	0.0921	comp	0.37	3.27	1.64	67.5
31	IRAS10565+2448	F10565+2448	105918.14+243234.3	0.0431	...	0.38	18.59	11.90	364.5
32	Mrk162	F11022+4501	110508.10+444447.0	0.0215	sb	0.30	0.53	0.78	12.9
33	ESO319-G022	F11255-4120	112754.18-413651.7	0.0164	...	0.30	5.17	4.49	106.7
34	Mrk1457	F11447+5243	114721.61+522658.0	0.0486	agn	0.29	3.37	3.77	66.4

Table 3—Continued

source	Name	FSC Name	J2000 coordinates	z ^a	SDSS ^b	EW(6.2 μ m) ^c μ m	f(6.2 μ m) ^d	f(11.3 μ m) ^e	f_{ν} (7.7 μ m) mJy
35	IRASF11553+4557	F11553+4557	115758.19+454024.0	0.1466	agn	0.10	0.83	1.12	35.0
36	IRAS12018+1941	F12018+1941	120424.53+192509.8	0.1686	agn	0.11	0.94	0.31	45.4 ^f
37	NGC4102	F12038+5259	120623.12+524239.0	0.0028	...	0.30	82.72	101.27	1784.4
38	IRAS12112+0305	F12112+0305	121346.05+024841.3	0.0733	sb	0.38	5.82	2.72	89.7
39	IRASF12388+3327	F12388+3327	124119.18+331112.0	0.0949	sb	0.32	2.30	1.35	46.4
40	IRASF13167+1336	F13167+1336	131913.94+132030.0	0.0962	agn	0.27	1.55	1.56	35.4
41	CGCG218-007	F13215+4333	132348.41+431804.0	0.0273	agn	0.25	3.46	4.25	81.3
42	NGC5135	F13229-2934	132543.97-295000.0	0.0137	...	0.39	39.86	38.59	755.0
43	IRASF13265+4411	F13265+4411	132844.06+435550.0	0.0279	sb	0.37	0.63	0.58	10.9
44	IRAS13469+5833	F13469+5833	134840.23+581851.9	0.1578	comp	0.18	0.69	0.71	21.6
45	IRASF14321+0543	F14321+0543	143437.88+053016.0	0.0847	agn	0.35	1.81	1.51	34.6
46	IRAS14378-3651	F14378-3651	144058.90-370433.0	0.0676	...	0.31	4.05	2.23	86.0
47	NGC5793	F14565-1629	145924.76-164136.0	0.0116	...	0.39	20.09	14.51	411.2
48	IRAS15001+1433	F15001+1433	150231.94+142135.3	0.1627	sb	0.14	1.94	1.34	61.5
49	IRAS15206+3342	F15206+3342	152238.12+333136.1	0.1244	sb	0.28	4.38	2.98	90.0
50	Arp220	F15327+2340	153457.24+233011.7	0.0181	agn	0.12	0.13	7.80	582.2 ^f
51	IRASF15553+2329	F15553+2329	155732.31+232050.0	0.0329	sb	0.35	0.63	0.64	10.8
52	Mrk883	F16277+2433	162952.85+242638.3	0.0375	comp	0.26	1.86	2.30	33.2
53	IRASF16305+4823	F16305+4823	163158.73+481722.0	0.0874	sb	0.17	2.09	1.40	77.1
54	IRAS16334+4630	F16333+4630	163452.37+462453.0	0.1910	...	0.30	1.32	1.06	31.0
55	IRASF16399-0937	F16399-0937	164240.11-094313.7	0.0270	...	0.17	4.26	6.01	167.2
56	IRAS16455+4553	F16455+4553	164658.90+454823.0	0.1906	...	0.13	0.57	0.59	27.5
57	IRAS16487+5447	F16487+5447	164946.88+544235.4	0.1038	...	0.29	2.03	1.40	46.5
58	NGC6240	F16504+0228	165258.89+022403.4	0.0245	...	0.24	28.88	22.87	584.1
59	IRASF16525+3322	F16525+3322	165423.52+331803.0	0.1348	sb	0.34	1.57	1.04	32.0
60	IRAS17028+5817	F17028+5817	170341.91+581344.4	0.1061	...	0.39	3.08	1.89	60.9
61	IRAS17208-0014	F17207-0014	172321.93-001700.4	0.0428	...	0.29	14.57	8.77	356.9
62	ESO138-G027	F17222-5953	172643.35-595555.2	0.0208	...	0.35	10.70	9.38	219.9
63	CGCG141-034	F17548+2401	175656.65+240102.0	0.0198	...	0.39	13.56	9.73	267.2
64	IC4734	F18341-5732	183825.75-572925.4	0.0156	...	0.38	23.80	18.08	449.1
65	IRAS18580+6527	F18580+6527	185813.90+653124.0	0.1764	...	0.35	2.15	1.74	36.8
66	IRAS19297-0406	F19297-0406	193221.25-035956.3	0.0857	...	0.30	4.59	2.90	95.8
67	ESO339-G011	F19542-3804	195737.60-375608.4	0.0192	...	0.19	8.71	9.17	303.2
68	IRAS20087-0308	F20087-0308	201123.86-025950.8	0.1057	...	0.24	4.96	2.83	123.1

Table 3—Continued

source	Name	FSC Name	J2000 coordinates	z^a	SDSS ^b	EW(6.2 μm) ^c μm	$f(6.2 \mu\text{m})^d$	$f(11.3 \mu\text{m})^e$	$f_\nu(7.7 \mu\text{m})$ mJy
69	IC5135	F21453-3511	214819.50-345706.0	0.0162	...	0.18	12.10	14.43	328.6
70	UGC11871	F21582+1018	220041.38+103308.7	0.0266	...	0.12	6.08	9.03	211.7
71	ESO602-G025	F22287-1917	223125.48-190204.0	0.0250	...	0.30	20.64	19.17	496.8
72	UGC12150	F22389+3359	224112.21+341456.8	0.0214	...	0.38	18.95	17.33	378.2
73	ESO239-IG002	F22467-4906	224939.84-485058.3	0.0430	...	0.31	6.99	6.10	142.5
74	CGCG453-062	F23024+1916	230456.55+193307.1	0.0251	...	0.38	8.58	6.91	184.5
75	IRAS23230-6926	F23230-6926	232603.57-691020.3	0.1063	...	0.20	2.00	1.30	68.5
76	IRAS23253-5415	F23253-5415	232806.10-535831.0	0.1300	...	0.15	0.93	0.90	28.0
77	Mrk930	F23294+2840	233158.30+285650.0	0.0183	...	0.14	0.39	0.74	10.9 ^f
78	IRAS23327+2913	F23327+2913	233511.93+293000.2	0.1070	...	0.18	1.09	0.81	29.5
79	IRAS23365+3604	F23365+3604	233901.29+362109.8	0.0645	...	0.27	4.43	2.70	116.2

^aRedshift from optical redshift in NED.

^bOur optical classification determined from spectra of the Sloan Digital Sky Survey, determined from presence of broad hydrogen emission lines or ratios among [OIII] λ 5007, H β , [NII] λ 6584, and H α .

^cRest frame equivalent width of 6.2 μm PAH feature fit with single gaussian on a linear continuum within rest wavelength range 5.5 μm to 6.9 μm .

^dTotal flux of PAH 6.2 μm feature fit with single gaussian on a linear continuum within rest wavelength range 5.5 μm to 6.9 μm in units of $10^{-20} \text{W cm}^{-2}$.

^eTotal flux of PAH 11.3 μm feature fit with single gaussian on a linear continuum within rest wavelength range 10.5 μm to 12.0 μm in units of $10^{-20} \text{W cm}^{-2}$.

^f $f_\nu(7.9 \mu\text{m})$ measured because continuum stronger than PAH peak $f_\nu(7.7 \mu\text{m})$.

Table 4. SEDs and Total Luminosities of Composite Sources

source	FSC Name	$f_\nu(25)$ IRS Jy	$f_\nu(8)^a$ Jy	$f_\nu(12)^b$ Jy	$f_\nu(18)^a$ Jy	$f_\nu(25)^b$ Jy	$f_\nu(60)^b$ Jy	$f_\nu(65)^a$ Jy	$f_\nu(90)^a$ Jy	$f_\nu(100)^b$ Jy	$f_\nu(140)^a$ Jy	$f_\nu(160)^a$ Jy	$f_\nu(1.25)^c$ mJy	$f_\nu(1.66)^c$ mJy	R ^d	L_{ir}^e log
1	F00006+2141	0.959	0.197	0.226	0.546	1.050	4.340	3.212	3.715	4.320	4.340	2.109	10.91	17.39	3.38	44.66
2	F00199-7426	0.265	...	0.105	...	0.326	4.160	3.948	4.403	6.420	5.416	4.198	2.84	4.09	9.06	45.90
3	F00392-7930	0.194	0.139	0.220	0.182	0.190	1.510	1.412	1.632	3.220	4.007	2.986	11	17.29	3.12	44.60
4	F00509-0902	0.385	...	0.313	0.204	0.529	2.610	2.631	3.135	3.800	3.745	2.577	5.6	6.98	7.39	44.39
5	F01173+1405	1.333	0.182	0.265	0.592	1.440	11.100	10.669	10.441	9.330	8.062	4.886	4.55	11.28	6.46	45.28
6	F01197+0044	0.275	...	0.110	0.306	0.378	2.700	2.258	2.320	4.450	2.971	2.953	0.92	0.90	8.65	45.27
7	F01364-1042	0.335	...	0.077	...	0.396	6.160	5.018	6.289	6.700	4.802	1.669	1.42	2.05	18.67	45.38
8	F01417+1651	0.936	...	0.139	0.324	0.947	12.600	11.711	13.123	13.300	7.740	6.470	6.46	8.71	23.36	45.19
9	F02411+0353	0.169	...	0.085	...	0.224	1.370	1.520	1.364	1.950	3.016	1.435	0.6	2.21	5.99	45.85
10	F02417-0857	0.192	...	0.102	...	0.237	1.970	1.668	1.768	2.270	2.956	1.061	0.99	1.40	13.55	45.09
11	F02437+2122	0.543	...	0.103	0.261	0.581	5.740	5.407	6.826	6.390	6.347	5.556	7.37	11.79	9.52	44.74
12	F02568+3637	2.001	0.297	0.447	1.089	2.260	11.000	10.222	11.545	12.100	8.268	7.577	28.69	42.06	5.46	44.51
13	F03229-0619	0.296	0.125	0.227	...	0.382	2.950	2.307	2.665	6.770	2.558	3.171	11.4	14.61	4.81	44.96
14	F03359+1523	0.519	...	0.129	0.210	0.596	6.200	6.304	6.510	6.840	7.008	3.688	2.04	2.93	12.69	45.14
15	F04001-1811	0.303	0.156	0.155	0.302	0.452	2.860	2.075	2.976	5.060	5.711	4.075	11.74	17.25	4.87	44.66
16	F04018-4332	0.129	...	0.094	...	0.172	1.040	0.356	0.735	2.950	...	0.764	3.54	3.50	19.28	42.44
17	F04103-2838	0.526	...	0.075	0.402	0.538	1.820	1.168	1.199	1.710	1.799	0.511	1.46	1.94	7.32	45.78
18	F04113-5117	0.071	...	0.081	...	0.074	2.090	3.230	14.57	45.83
19	F04118-3207	1.959	0.390	0.525	1.100	2.130	14.200	12.360	16.278	21.600	17.946	16.168	16.71	20.77	5.03	44.62
20	F06076-2139	0.570	...	0.102	0.258	0.577	6.250	5.938	6.240	8.570	7.870	6.095	3.67	5.73	11.51	45.21
21	F06301-7934	0.072	...	0.042	...	0.087	1.920	2.180	1.936	2.140	2.149	...	0.59	0.80	18.77	45.95
22	F06456+6054	1.170	0.326	0.400	0.899	1.360	6.020	6.429	6.772	10.000	7.723	7.094	26.36	37.98	3.57	43.74
23	F08043+3909	0.428	...	0.188	0.209	0.405	1.280	0.772	1.145	1.430	0.855	...	8.46	10.17	9.35	44.30
24	F08273+5543	0.127	...	0.086	...	0.146	1.410	1.470	1.162	1.740	1.584	0.159	1.72	2.23	20.71	44.77
25	F08344+5105	0.128	...	0.071	...	0.133	2.140	2.311	2.000	2.690	2.622	...	0.83	1.28	8.67	45.59
26	F08580+6020	0.252	0.106	0.144	...	0.252	2.160	1.982	2.010	2.970	3.466	0.544	16.92	26.25	3.79	43.75
27	F10388+4033	0.260	...	0.087	...	0.274	1.310	1.245	0.950	1.350	1.703	0.852	1.32	1.59	16.35	45.16
28	F10398+1455	0.253	...	0.090	...	0.214	0.484	0.321	0.533	0.675	1.272	0.607	1.35	1.47	6.17	45.25
29	F10439+1400	0.786	0.168	0.476	0.606	1.090	6.010	3.442	6.893	12.600	12.396	9.904	6.62	7.99	27.59	44.20
30	F10494+4424	0.131	...	0.117	...	0.165	3.530	3.392	3.528	5.410	4.111	2.958	1.02	1.92	12.67	45.78
31	F10565+2448	0.997	0.131	0.217	0.452	1.140	12.100	11.808	13.816	15.100	11.819	6.473	7.69	11.59	7.29	45.61
32	F11022+4501	0.147	...	0.092	...	0.212	1.290	1.143	0.993	1.580	1.760	0.155	1.45	1.45	26.49	44.12
33	F11255-4120	0.724	...	0.204	0.324	0.811	8.060	6.594	8.559	8.410	7.744	7.391	4.45	6.58	15.90	44.58
34	F11447+5243	0.162	...	0.117	...	0.194	0.873	0.224	0.798	1.340	1.418	0.160	6	6.79	4.50	44.77

Table 4—Continued

source	FSC Name	$f_{\nu}(25)$ IRS Jy	$f_{\nu}(8)^a$ Jy	$f_{\nu}(12)^b$ Jy	$f_{\nu}(18)^a$ Jy	$f_{\nu}(25)^b$ Jy	$f_{\nu}(60)^b$ Jy	$f_{\nu}(65)^a$ Jy	$f_{\nu}(90)^a$ Jy	$f_{\nu}(100)^b$ Jy	$f_{\nu}(140)^a$ Jy	$f_{\nu}(160)^a$ Jy	$f_{\nu}(1.25)^c$ mJy	$f_{\nu}(1.66)^c$ mJy	R ^d	L_{ir}^e log
35	F11553+4557	0.187	...	0.097	...	0.200	0.799	0.567	0.789	0.838	0.158	1.212	1.39	1.74	7.92	45.70
36	F12018+1941	0.305	...	0.107	...	0.373	1.760	1.623	1.243	1.780	1.189	0.792	0.59	0.75	11.82 ^f	46.09
37	F12038+5259	5.535	1.082	1.510	3.287	6.760	46.900	50.127	54.050	69.700	48.746	51.257	72.39	125.63	6.39	43.88
38	F12112+0305	0.383	...	0.110	...	0.509	8.500	7.100	8.690	9.980	6.174	3.902	1.11	1.81	19.91	45.90
39	F12388+3327	0.157	...	0.086	...	0.194	0.966	0.769	0.798	1.180	0.980	...	0.9	1.18	6.36	45.34
40	F13167+1336	0.222	...	0.122	...	0.274	1.570	1.849	1.683	2.250	1.535	1.541	1.96	2.58	13.39	45.56
41	F13215+4333	0.195	...	0.081	...	0.269	1.360	1.778	1.280	2.390	1.735	...	7.69	11.67	4.89	44.39
42	F13229-2934	1.783	0.450	0.638	1.135	2.400	16.900	16.281	22.529	28.600	29.143	21.480	16.91	21.20	5.78	44.83
43	F13265+4411	0.095	...	0.115	...	0.133	0.525	0.709	0.83	0.89	18.73	44.12
44	F13469+5833	0.051	...	0.052	...	0.072	1.270	0.531	1.360	1.730	0.925	1.257	0.6	0.89	15.04	45.83
45	F14321+0543	0.102	...	0.070	...	0.136	0.818	0.565	0.795	1.150	1.672	...	1.44	1.93	7.11	45.17
46	F14378-3651	0.422	...	0.116	0.185	0.525	6.190	5.110	6.037	6.340	5.490	2.039	1.99	3.04	15.25	45.70
47	F14565-1629	0.500	0.157	0.190	0.202	0.592	6.210	6.044	8.828	8.960	9.541	6.931	15.95	25.72	3.48	44.21
48	F15001+1433	0.189	...	0.122	...	0.167	1.870	0.257	1.686	2.040	2.374	0.769	1.18	1.57	8.19	46.05
49	F15206+3342	0.339	...	0.081	0.194	0.347	1.770	0.906	1.259	1.890	1.224	...	1.53	1.70	13.39	45.80
50	F15327+2340	6.966	0.249	0.484	2.261	7.910	104.00	138.58	91.23	112.00	62.81	70.53	5.9	11.62	35.45 ^f	45.74
51	F15553+2329	0.093	...	0.090	...	0.103	0.483	...	0.545	0.975	0.907	...	0.81	0.74	17.53	44.23
52	F16277+2433	0.206	...	0.088	0.132	0.217	1.020	1.380	0.843	1.140	0.849	0.668	7.4	9.43	8.76	44.53
53	F16305+4833	0.164	...	0.099	...	0.212	2.070	1.639	1.777	2.340	2.526	2.725	1.49	1.89	6.59	45.51
54	F16333+4630	0.069	...	0.057	...	0.096	1.190	1.519	1.182	2.090	1.492	...	0.62	0.84	11.41	46.03
55	F16399-0937	0.890	0.221	0.236	0.403	1.080	7.990	7.342	9.316	12.500	10.888	5.820	2.95	4.65	11.88	45.08
56	F16455+4553	0.059	...	0.057	...	0.084	0.943	0.305	0.906	1.590	1.830	1.071	0.4	0.57	10.45	45.94
57	F16487+5447	0.173	...	0.074	...	0.201	2.880	2.926	2.316	3.070	2.432	1.345	1.03	2.08	13.75	45.76
58	F16504+0228	3.037	0.350	0.558	1.489	3.420	22.700	25.656	23.179	27.800	21.087	18.302	26.67	33.85	9.04	45.42
59	F16525+3322	0.098	...	0.071	...	0.117	0.783	0.728	0.684	1.550	0.46	0.86	8.41	45.61
60	F17028+5817	0.102	...	0.059	...	0.104	2.430	2.715	2.458	3.910	3.824	3.015	0.87	1.46	9.66	45.74
61	F17207-0014	1.436	0.119	0.195	0.477	1.660	31.100	34.466	29.648	34.900	23.687	19.251	4.39	7.62	17.05	45.97
62	F17222-5953	1.039	0.211	0.355	0.605	1.310	9.840	7.704	10.722	11.600	11.298	7.804	5.23	7.81	10.41	44.91
63	F17548+2401	0.482	0.096	0.163	0.267	0.542	6.280	6.568	7.865	9.890	9.124	2.933	8.27	13.12	5.48	44.68
64	F18341-5732	1.038	0.240	0.374	0.574	1.270	14.400	13.608	17.919	25.200	16.182	18.967	11.6	18.08	7.73	44.85
65	F18580+6527	0.065	...	0.046	...	0.065	0.763	0.732	0.759	1.400	1.311	0.962	1.03	1.17	6.39	45.79
66	F19297-0406	0.430	...	0.126	...	0.589	7.050	7.720	5.65	5.70	16.05	45.97
67	F19542-3804	0.884	0.248	0.374	0.603	1.170	6.050	5.872	7.621	9.140	10.184	8.507	12.83	12.84	5.56	44.71
68	F20087-0308	0.182	...	0.129	...	0.243	4.700	4.193	5.721	6.540	4.560	4.331	1.67	2.84	8.99	46.01

Table 4—Continued

source	FSC Name	$f_\nu(25)$ IRS Jy	$f_\nu(8)$ ^a Jy	$f_\nu(12)$ ^b Jy	$f_\nu(18)$ ^a Jy	$f_\nu(25)$ ^b Jy	$f_\nu(60)$ ^b Jy	$f_\nu(65)$ ^a Jy	$f_\nu(90)$ ^a Jy	$f_\nu(100)$ ^b Jy	$f_\nu(140)$ ^a Jy	$f_\nu(160)$ ^a Jy	$f_\nu(1.25)$ ^c mJy	$f_\nu(1.66)$ ^c mJy	R ^d	L_{ir} ^e log
69	F21453-3511	1.608	0.405	0.588	1.108	2.120	16.500	15.829	19.116	25.600	25.342	16.793	12.9	15.48	12.43	44.95
70	F21582+1018	0.487	0.146	0.187	0.320	0.513	4.150	3.609	5.040	6.740	6.992	5.122	7.86	11.36	5.07	44.80
71	F22287-1917	0.638	0.224	0.291	0.375	0.763	5.970	5.520	7.421	10.200	10.919	8.942	8.74	12.16	3.19	44.92
72	F22389+3359	0.791	0.180	0.363	0.422	0.794	8.170	7.593	10.289	14.200	12.904	11.890	11.34	17.62	5.52	44.90
73	F22467-4906	0.960	...	0.128	0.414	1.050	6.660	6.925	6.401	7.930	6.484	4.905	6.03	8.32	10.91	45.38
74	F23024+1916	0.397	0.163	0.201	0.240	0.529	7.530	6.610	8.049	10.600	9.766	8.366	8.91	8.10	9.10	44.94
75	F23230-6926	0.287	...	0.059	...	0.295	3.740	3.114	2.855	3.420	3.022	0.701	1.13	1.44	11.48	45.87
76	F23253-5415	0.180	...	0.064	...	0.214	2.300	2.347	2.321	3.490	3.251	2.512	1.39	2.10	21.24	45.92
77	F23294+2840	0.164	...	0.079	...	0.232	1.250	0.932	0.983	2.150	1.969	33.81 ^f	44.00
78	F23327+2913	0.209	...	0.058	...	0.225	2.100	1.620	1.740	2.810	2.178	1.997	1	1.55	17.63	45.69
79	F23365+3604	0.659	...	0.096	0.279	0.808	7.090	6.702	6.867	8.360	5.963	5.436	2.56	3.88	13.59	45.74

^aFlux densities at listed wavelengths taken from AKARI catalog, <http://darts.isas.jaxa.jp/astro/akari/cas/tools/search/crossid.html>.

^bFlux densities at listed wavelengths taken from IRAS Faint Source Catalog, <http://vizier.u-strasbg.fr/viz-bin/VizieR-4>.

^cFlux densities at listed wavelengths taken from 2MASS catalog.

^dRatio $R = f_{IR}/\nu f_\nu(7.7 \mu\text{m})$, for $f_{IR} = 1.8 \times 10^{-11}[13.48f_\nu(12) + 5.16f_\nu(25) + 2.58f_\nu(60) + f_\nu(100)]$ in $\text{erg cm}^{-2} \text{s}^{-1}$.

^eTotal infrared luminosity $L_{ir} = 4\pi D^2 f_{IR}$ in erg s^{-1} for D the luminosity distance determined for $H_0 = 71 \text{ km s}^{-1} \text{Mpc}^{-1}$, $\Omega_M=0.27$ and $\Omega_\Lambda=0.73$, from Wright (2006): <http://www.astro.ucla.edu/~wright/CosmoCalc.html>.

^f $f_\nu(7.9\mu\text{m})$ measured for ratio because continuum stronger than PAH peak $f_\nu(7.7 \mu\text{m})$.

Table 5. Spectroscopic Properties of AGN

source	Name	FSC Name	J2000 coordinates	z^a	SDSS ^b	EW(6.2 μm) ^c	f(6.2 μm) ^d	f(11.3 μm) ^e	$f_\nu(7.7 \mu\text{m})$ mJy	silicate ^f
1	IRAS00275-2859	F00275-2859	003004.20-284225.4	0.2781	...	0.011	0.22	0.19	63.4 ^g	0.71
2	IRAS00406-3127	F00406-3127	004303.14-311049.7	0.3424	...	<0.011	<0.08	0.24	34.5 ^g	0.15
3	IZw1	F00509+1225	005334.94+124136.2	0.0611	...	<0.003	<0.48	1.25	294.6 ^g	1.27
4	IRAS01003-2238	F01004-2237	010249.94-222157.3	0.1177	...	<0.043	<0.99	0.28	106.5 ^g	0.47
5	NGC454	F01123-5539	011424.90-552352.0	0.0122	...	<0.008	<0.66	3.16	130.5	P+abs
6	IRAS01199-2307	F01199-2307	012220.84-225157.3	0.1560	...	<0.088	<0.41	0.22	24.1 ^g	0.03
7	NGC526a	F01216-3519	012354.39-350355.0	0.0191	...	<0.001	<0.08	<0.08	112.9	...
8	3C48	F01348+3254	013741.29+330935.0	0.3670	...	0.006	0.31	0.25	60.5	...
9	ESO297-018	F01364-4016	013837.16-400041.0	0.0252	...	0.024	0.47	1.25	46.8	0.75
10	IRAS01569-2939	F01569-2939	015913.79-292434.5	0.1363 ^h	...	<0.029	<0.51	0.53	33.8 ^g	0.06
11	Mrk1014	F01572+0009	015950.23+002340.5	0.1630	agn	0.036	1.12	1.37	77.9	...
12	NGC788	F01586-0703	020106.45-064855.9	0.0136	...	<0.003	<0.08	0.64	80.1	0.79
13	IRAS02054+0835	F02054+0835	020806.90+085004.3	0.3450	...	0.024	0.40	0.40	52.8	P+abs
14	Mrk590	F02120-0059	021433.56-004600.1	0.0264	...	<0.007	<0.13	0.30	40 ^g	1.09
15	IRASF02132-1524	F02132-1524	021538.50-151013.9	0.2110	...	<0.005	<0.19	<0.03	50.2 ^g	...
16	UM420	F02183+0019	022053.40+003324.3	0.0584	...	0.031	0.32	0.11	27 ^g	0.22
17	2MASSJ022150.60+132741.0	F02191+1313	022150.60+132741.0	0.1400	...	<0.007	<0.18	<0.27	30.8 ^g	0.78
18	IC1816	F02297-3653	023151.00-364019.4	0.0169	...	0.031	0.81	2.57	70.3	0.63
19	NGC973	F02313+3217	023420.11+323020.2	0.0162	...	<0.002	<0.06	0.84	73.6	0.44
20	IRAS03158+4227	F03158+4227	031911.97+423825.7	0.1344	...	<0.034	<0.67	0.49	78.5 ^g	0.03
21	NGC1386	F03348-3609	033646.20-355957.0	0.0029	...	<0.001	<0.13	4.33	377.8	0.48
22	ESO548-G81	F03398-2123	034203.72-211439.0	0.0145	...	<0.002	<0.34	1.24	103.4 ^g	1.23
23	IRAS03450+0055	F03450+0055	034740.18+010514.0	0.0310	...	<0.001	<0.1	<0.7	153 ^g	1.12
24	IRAS03538-6432	F03538-6432	035425.23-642344.5	0.3007	...	0.079	0.69	0.71	36.4 ^g	P+abs
25	ESO157-G023	F04213-5620	042224.18-561333.5	0.0435	...	<0.002	<0.05	<0.11	28.8 ^g	1.06
26	3C120	F04305+0514	043311.10+052115.6	0.0330	...	<0.001	<0.05	0.68	181.5	1.12
27	IRAS04313-1649	F04313-1649	043337.08-164331.5	0.2680	...	<0.046	<0.11	0.18	14.2 ^g	0.05
28	ESO203-IG001	F04454-4838	044649.55-483330.6	0.0529	...	<0.029	<0.43	0.45	65 ^g	0.02
29	CGCG420-015	F04507+0358	045325.75+040341.7	0.0294	...	<0.003	<0.21	0.71	193.0	...
30	Ark120	F05136-0012	051611.42-000859.4	0.0327	...	<0.001	<0.13	1.33	214.2	1.24
31	IRAS05189-2524	F05189-2524	052101.41-252145.5	0.0426	...	0.017	3.74	5.05	491.1	P+abs
32	GAM-0521-365	F05212-3630	052257.98-362730.0	0.0553	...	<0.004	<0.1	<0.04	58.2 ^g	1.08
33	2MASXJ05580206-3820043	F05563-3820	055802.00-382004.0	0.0339	...	<0.001	<0.63	<0.36	392.4 ^g	0.83
34	PKS0558-504	F05585-5026	055947.37-502651.8	0.1372	...	<0.005	<0.07	0.49	38.5 ^g	1.27

Table 5—Continued

source	Name	FSC Name	J2000 coordinates	z^a	SDSS ^b	EW(6.2 μm) ^c μm	$f(6.2 \mu\text{m})^d$	$f(11.3 \mu\text{m})^e$	$f_\nu(7.7 \mu\text{m})$ mJy	silicate ^f
35	IRAS06035-7102	F06035-7102	060253.63-710311.9	0.0795	...	<0.076	<3.83	2.40	153.5	P+abs
36	IRAS06206-6315	F06206-6315	062100.80-631723.2	0.0924	...	<0.107	<1.55	1.05	65.2	P+abs
37	ESO121-IG028	F06230-6057	062345.57-605844.0	0.0405	...	<0.013	<0.05	<0.08	8.7 ^g	0.61
38	UGC3478	F06279+6342	063247.17+634025.0	0.0128	...	0.047	1.73	2.41	93.3	...
39	IRAS06361-6217	F06361-6217	063635.71-622031.8	0.1596	...	0.052	1.17	0.42	63.7 ^g	0.07
40	IRASF07260+3955	F07260+3955	072930.29+394941.0	0.0788	sb	0.032	0.50	0.34	34.9 ^g	0.22
41	Mrk9	F07327+5852	073657.00+584613.0	0.0399	...	<0.142	<8.12	3.54	162.5	1.05
42	IRASF07546+3928	F07546+3928	075800.05+392029.1	0.0960	...	<0.005	<0.21	<0.14	98.5	1.17
43	2MASXJ08022436+4643008	F07588+4651	080224.33+464300.8	0.1208	agn	<0.001	<0.02	0.40	42.8	0.65
44	IRAS07598+6508	F07599+6508	080430.46+645952.9	0.1488	...	0.005	0.59	0.30	217.2	1.09
45	2MASXJ08244333+2959238	F08216+3009	082443.28+295923.0	0.0253	comp	0.001	0.21	0.65	114.1	...
46	ESO60-IG016	F08520-6850	085232.07-690154.8	0.0451	...	0.070	5.55	3.31	241.9 ^g	P+abs
47	IRAS08572+3915	F08572+3915	090025.38+390354.3	0.0584	sb	<0.001	<0.24	...	649.1 ^g	0.02
48	SBS0915+556	F09155+5541	091913.19+552755.3	0.0494	agn	<0.003	<0.03	<0.11	26.7	...
49	MCG-01-24-012	F09182-0750	092046.25-080322.1	0.0196	...	<0.005	<0.13	0.69	67.9	0.58
50	Mrk705	F09233+1257	092603.29+124403.6	0.0292	agn	0.018	0.62	1.33	84.1	...
51	UGC5101	F09320+6134	093551.65+612111.3	0.0394	agn	<0.121	<6.77	6.73	290.9	P+abs
52	IRASF09414+4843	F09414+4843	094442.24+482916.0	0.0553	agn	0.065	0.82	1.09	49.7	P+abs
53	3C234	F09589+2901	100149.55+284709.3	0.1849	agn	<0.001	<0.04	<0.04	104.2	...
54	IRASF10038-3338	F10038-3338	100604.65-335306.1	0.0342	...	<0.002	<0.69	3.55	843.9 ^g	0.03
55	IRASF10036+4136	F10036+4136	100642.59+412201.0	0.1498	agn	0.047	0.35	0.78	25.8	...
56	ESO374-G044	F10111-3544	101319.91-355857.7	0.0285	...	<0.006	<0.05	0.23	41.2	...
57	Mrk141	F10156+6413	101912.56+635803.0	0.0417	agn	0.055	1.22	1.53	61.9	...
58	NGC3227	F10207+2007	102330.60+195154.0	0.0039	...	0.093	15.03	21.35	484.8	P+abs
59	IRAS10378+1109	F10378+1108	104029.17+105317.7	0.1363	agn	<0.078	<0.45	0.36	35.5 ^g	0.09
60	NGC3393	F10459-2453	104823.39-250942.8	0.0125	...	<0.003	<0.05	0.64	69.5	...
61	IRASF10590+6515	F10590+6515	110213.02+645924.0	0.0775	agn	0.022	0.58	1.35	49.7	P+abs
62	IRAS11095-0238	F11095-0238	111203.34-025424.1	0.1066	...	<0.027	<0.85	0.54	119.9 ^g	0.03
63	IRAS11119+3257	F11119+3257	111438.88+324133.1	0.1890	...	0.014	0.89	0.83	124.5 ^g	0.53
64	IRASF11233+3451	F11233+3451	112602.45+343448.0	0.1108	comp	0.052	1.26	1.36	66.1	...
65	SBS1133+572	F11330+5713	113549.06+565708.0	0.0507	agn	0.040	2.28	3.41	144.9	P+abs
66	NGC3783	F11365-3727	113901.78-374418.7	0.0112 ^a	...	<0.001	<0.31	1.44	404.0	...
67	LEDA088639	F11431-1810	114540.47-182715.0	0.0329	...	<0.001	<0.04	0.08	46.2	1.15
68	POX4	F11486-2019	115111.60-203602.0	0.0120	...	<0.003	<0.03	0.08	5.8 ^g	...

Table 5—Continued

source	Name	FSC Name	J2000 coordinates	z^a	SDSS ^b	EW(6.2 μm) ^c μm	$f(6.2 \mu\text{m})^d$	$f(11.3 \mu\text{m})^e$	$f_\nu(7.7 \mu\text{m})$ mJy	silicate ^f
69	UM462	F11500-0211	115237.30-022810.0	0.0035	...	<0.026	<0.06	0.22	5.5	...
70	IRASF11513+6155	F11513+6155	115402.05+613844.0	0.1467	agn	<0.003	<0.05	0.10	41.5 ^g	0.34
71	CGCG041-020	F11583+0705	120057.92+064823.0	0.0360	agn	0.070	1.11	1.70	54.3	P+abs
72	UGC7064	F12021+3126	120443.34+311038.2	0.0250	agn	0.081	2.00	3.12	84.6	...
73	IRAS12072-0444	F12072-0444	120945.12-050113.9	0.1284	...	0.051	0.92	0.59	72.6 ^g	0.22
74	NGC4151	Z12080+3940	121032.60+392421.0	0.0033	...	<0.011	<6.91	4.82	1187.5	1.03
75	IRAS12127-1412	F12127-1412	121519.14-142941.4	0.1330	...	<0.004	<0.15	0.17	72.7 ^g	0.09
76	NGC4507	F12329-3938	123536.55-395433.3	0.0118	...	<0.002	<0.31	4.60	422.2	...
77	ESO506-G027	F12362-2702	123854.59-271828.0	0.0250	...	<0.001	<0.09	0.57	156.5 ^g	0.33
78	PG1244+026	F12440+0238	124635.24+022208.7	0.0482	comp	0.017	0.22	0.31	28.4	...
79	2MASX J12485992-0109353	F12464-0053	124859.92-010935.4	0.0886	agn	<0.029	<0.23	0.46	22 ^g	1.17
80	SDSSJ125306.00-031258.9	F12505-0256	125306.00-031258.9	0.0227	...	<0.002	<0.02	0.23	45.3	...
81	IRAS12514+1027	F12514+1027	125400.82+101112.4	0.3182 ^h	...	<0.009	<0.3	0.39	68.7 ^g	0.23
82	Mrk231	F12540+5708	125614.29+565225.1	0.0422	...	0.007	4.06	3.71	1585.7 ^g	0.47
83	NGC4941	F13016-0517	130413.10-053306.0	0.0037	...	<0.041	<1.06	0.82	55.0	0.92
84	ESO323-077	F13036-4008	130626.13-402452.0	0.0150	...	0.029	8.64	12.34	563.3	...
85	MCG-03-34-064	F13197-1627	132224.45-164342.4	0.0165	...	<0.001	<0.17	3.63	552.5	0.77
86	IRAS13218+0552	F13218+0552	132419.81+053704.6	0.2051	...	0.003	0.30	0.14	270.2 ^g	0.60
87	IRASF13279+3401	F13279+3402	133015.23+334629.4	0.0213 ^h	...	0.038	0.24	0.35	24.4 ^g	0.07
88	M-6-30-15	F13330-3402	133554.54-341750.4	0.0077	...	<0.001	<0.15	2.20	235.5 ^g	...
89	IRAS13342+3932	F13342+3932	133624.07+391730.1	0.1793	agn	0.073	1.33	1.04	61.9	...
90	IRAS13352+6402	F13352+6402	133651.15+634704.7	0.2366	...	0.076	0.77	0.50	40.4	P+abs
91	IRAS13349+2438	F13349+2438	133718.73+242303.3	0.1076	...	<0.001	<0.13	0.44	450.1 ^g	1.10
92	Mrk273	F13428+5608	134442.12+555313.1	0.0378	comp	0.088	7.52	5.34	337.2	...
93	2MASXJ13463217+6423247	F13450+6437	134632.14+642325.0	0.0242	agn	<0.045	<0.24	0.55	9.4	...
94	IRAS13451+1232	F13451+1232	134733.36+121724.2	0.1217	agn	<0.003	<0.07	<0.62	56.1	0.67
95	IC4329a	F13464-3003	134919.29-301834.4	0.0161	...	<0.001	<0.37	<1.72	809.7	...
96	NGC5347	F13510+3344	135317.83+332927.0	0.0078	agn	0.025	1.13	2.93	138.3	0.76
97	Mrk463E	F13536+1836	135602.90+182219.0	0.0500	sb	<0.001	<0.12	1.07	412.1	0.66
98	IRAS14026+4341	F14026+4341	140438.72+432707.3	0.3233	agn	0.011	0.41	0.43	56.6 ^g	0.90
99	PG1402+261	F14029+2610	140516.24+255533.7	0.1640	...	<0.003	<0.09	0.26	52.6 ^g	1.22
100	IRASF14036+4040	F14036+4040	140541.21+402632.0	0.0805	agn	0.018	0.21	0.55	38.7	...
101	OQ+208	F14047+2841	140700.39+282714.0	0.0766	agn	0.018	1.06	1.68	97.1	1.33
102	NGC5506	F14106-0258	141314.87-031227.0	0.0062	agn	<0.007	<5.41	11.28	1191.4	0.43

Table 5—Continued

source	Name	FSC Name	J2000 coordinates	z ^a	SDSS ^b	EW(6.2 μm) ^c μm	f(6.2 μm) ^d	f(11.3 μm) ^e	f_ν (7.7 μm) mJy	silicate ^f
103	NGC5548	F14157+2522	141759.53+250812.4	0.0172	agn	0.024	1.30	2.26	135.0	...
104	ESO511-G030	F14164-2625	141922.42-263841.0	0.0224	...	<0.001	<0.6	0.29	45.4 ^g	1.37
105	OQ530	F14180+5437	141946.59+542314.0	0.1526	agn	<0.001	<0.04	<0.08	49 ^g	...
106	PG1426+015	F14265+0130	142906.59+011706.5	0.0865	...	<0.002	<0.11	0.32	74.6	1.16
107	IRAS14348-1447	F14348-1447	143738.27-150024.6	0.0827	...	<0.174	<2.65	2.24	91.7	P+abs
108	TOLOLO1437+030	F14376+0300	144012.70+024743.5	0.0298	comp	0.064	0.27	0.41	12.3 ^g	...
109	Mrk477	F14390+5343	144038.09+533015.0	0.0377	comp	0.031	0.89	1.74	88.9	...
110	PG1440+356	F14400+3539	144207.46+352622.9	0.0791	...	0.017	0.99	1.34	79.1	...
111	NGC5728	F14396-1702	144223.93-171511.0	0.0094	...	0.077	4.00	10.68	234.4	...
112	IRASF14463+3612	F14463+3612	144825.10+355946.0	0.1131	agn	<0.02	<0.15	0.32	19.9	...
113	IRASF14474+4233	F14474+4233	144920.72+422101.0	0.1783	agn	<0.001	<0.07	<0.29	80.0	0.89
114	IRASF14541+4906	F14541+4906	145549.42+485436.0	0.2459	comp	<0.004	<0.06	<0.16	49 ^g	0.54
115	2MASSJ150113.21+232908.3	F14589+2340	150113.21+232908.3	0.2580	agn	<0.012	<0.07	<0.09	17.9 ^g	0.87
116	Mrk1392	F15034+0353	150556.55+034226.3	0.0361	agn	<0.008	<0.1	0.31	51.0	...
117	IRASF15065+0446	F15065+0446	150904.22+043441.0	0.1116	agn	0.085	0.54	0.74	29.7	...
118	2MASSJ151653.24+190048.4	F15146+1911	151653.24+190048.4	0.1900	...	<0.003	<0.18	<0.13	93.6 ^g	1.22
119	IRASF15176+5216	F15176+5216	151907.33+520606.0	0.1391	agn	0.034	1.04	1.11	71.7	...
120	IRAS15225+2350	F15225+2350	152443.94+234010.2	0.1390	sb	0.051	0.61	0.48	42.4 ^g	0.09
121	IRAS15250+3609	F15250+3608	152659.40+355837.5	0.0552	sb	<0.034	<0.12	1.62	242.6 ^g	0.04
122	3C321	F15295+2414	153143.45+240419.1	0.0961	...	<0.018	<0.08	0.26	59.0	0.44
123	2MASXJ15401288+5609463	F15390+5619	154012.91+560946.7	0.0740	agn	0.064	0.99	1.12	42.5	P+abs
124	PG1543+489	F15439+4855	154530.20+484609.0	0.3996	agn	0.007	0.10	<0.06	41.1 ^g	...
125	IRASF15456+5506	F15456+5506	154653.53+545706.0	0.1076	comp	0.006	0.23	<0.06	61.9	...
126	SBS1609+490	F16094+4902	161051.78+485439.0	0.0451	agn	<0.005	<0.04	0.18	20.8	0.64
127	IRAS16090-0139	F16090-0139	161140.42-014705.8	0.1336	...	<0.057	<1.58	1.19	96.3 ^g	0.08
128	PG1613+658	F16136+6550	161357.18+654309.6	0.1290	...	0.010	0.42	0.97	83.3	...
129	PG1612+261	F16121+2611	161413.21+260416.4	0.1309	agn	<0.001	<0.02	0.23	34.8	...
130	2MASXJ16164729+3716209	F16149+3723	161647.31+371621.0	0.1518	comp	<0.009	<0.06	0.18	20.0	...
131	IRASF16328+2055	F16328+2055	163459.83+204936.0	0.1285	agn	0.036	0.82	0.75	48.6	...
132	IRASF16463+3027	F16463+3027	164819.02+302210.0	0.1023	agn	<0.003	<0.06	<0.02	43.4	0.80
133	2MASSJ165939.77+183436.9	F16574+1838	165939.77+183436.9	0.1707	agn	0.016	0.32	0.40	54.3	...
134	PG1700+518	F17002+5153	170124.91+514920.4	0.2920	...	<0.009	<0.36	0.73	86 ^g	1.13
135	IRAS17044+6720	F17044+6720	170428.41+671628.5	0.1350	...	0.040	1.02	0.51	70.8 ^g	0.17
136	3C351	F17040+6048	170441.37+604430.5	0.3719	agn	<0.007	<0.11	<0.05	34.5	1.09

Table 5—Continued

source	Name	FSC Name	J2000 coordinates	z^a	SDSS ^b	EW(6.2 μm) ^c μm	f(6.2 μm) ^d	f(11.3 μm) ^e	$f_\nu(7.7 \mu\text{m})$ mJy	silicate ^f
137	IRAS17068+4027	F17068+4027	170832.12+402328.2	0.1790	...	<0.079	<0.78	0.70	49.2 ^g	0.12
138	2MASXJ17135038+5729546	F17130+5733	171350.32+572955.2	0.1130	agn	<0.004	<0.06	0.14	34.7	0.72
139	IRASF17341+5704 ⁱ	F17341+5704	173501.25+570308.0	0.0472	sb	<0.008	<0.03	<0.12	13.4	...
140	3C371	F18072+6948	180650.68+694928.0	0.0510	...	<0.001	<0.07	<0.1	79.2 ^g	...
141	H1821+643	F18216+6419A	182157.31+642036.3	0.2970	...	<0.002	<0.2	0.74	158.9	1.11
142	3C382	F18332+3239	183503.42+324146.1	0.0579	...	<0.001	<0.09	<0.02	94.5 ^g	1.18
143	IRAS18325-5926	F18325-5926	183658.29-592408.6	0.0200	...	0.020	3.99	7.13	454.8	P+abs
144	ESO103-g035	F18333-6528	183820.30-652540.0	0.0133	...	<0.003	<0.68	<0.16	393.0	0.43
145	3C390.3	F18456+7943	184208.98+794617.0	0.0561	...	<0.001	<0.04	<0.02	66.8	1.06
146	IRAS18443+7433	F18443+7433	184254.80+743621.0	0.1347	...	<0.051	<0.75	0.37	56.2 ^g	0.04
147	ESO140-G043	F18402-6224	184453.98-622153.4	0.0142	...	0.022	3.25	6.89	294.1	1.09
148	H1846-786	F18389-7834	184703.20-783151.0	0.0741	...	<0.012	<0.12	0.39	39.3 ^g	0.92
149	ESO141-G055	F19169-5845	192114.15-584013.1	0.0371	...	<0.003	<0.23	0.75	123.9 ^g	1.22
150	IRAS19254-7245south	F19254-7245	193121.55-723922.0	0.0617	...	<0.032	<3.08	4.19	229.7 ^g	0.26
151	IRAS20037-1547	F20036-1547	200631.70-153908.0	0.1919	...	0.043	1.41	0.97	79.1	...
152	NGC6860	F20045-6114	200846.90-610601.0	0.0149	...	0.084	6.32	3.59	162.5	1.01
153	IRAS20100-4156	F20100-4156	201329.85-414734.7	0.1296	...	<0.144	<1.68	1.27	88.7 ^g	0.06
154	IRAS20210+1121	F20210+1121	202325.37+113135.0	0.0564	...	<0.032	<1.4	3.10	182.1	0.69
155	Mrk509	F20414-1054	204409.74-104324.5	0.0344	...	0.017	2.29	3.29	229.5	...
156	IRAS20460+1925	F20460+1925	204817.23+193655.0	0.1807	...	<0.002	<0.26	<0.22	202.9	0.85
157	IC5063	F20482-5715	205202.30-570408.0	0.0113	...	<0.002	<0.48	0.82	539.3	0.72
158	IRAS20551-4250	F20551-4250	205826.78-423901.6	0.0430	...	0.063	4.10	3.11	294.3 ^g	0.05
159	Tol2138-405	F21382-4032	214121.80-401908.0	0.0581	...	<0.011	<0.05	<0.03	7 ^g	...
160	PHL1811	F21523-0936	215501.48-092224.0	0.1900	...	0.005	0.19	0.12	87.2 ^g	1.20
161	NGC7172	F21591-3206	220201.90-315211.0	0.0087	...	0.027	6.04	4.52	399.4	P+abs
162	BLLac	F22006+4202	220243.29+421639.0	0.0686	...	<0.002	<0.64	<0.08	163.4 ^g	...
163	NGC7212	F22045+0959	220701.95+101401.0	0.0267	...	<0.013	<0.21	1.59	98.0	0.62
164	NGC7213	F22061-4724	220916.25-471000.0	0.0058	...	<0.005	<0.37	2.53	117.7 ^g	1.48
165	3C445	F22212-0221	222349.57-020612.4	0.0562	...	<0.002	<0.11	<0.05	118.6 ^g	1.24
166	Mrk915	F22341-1248	223646.50-123242.6	0.0241	...	<0.004	<0.06	0.39	44.7	...
167	UGC12138	F22377+0747	224017.05+080314.1	0.0250	...	0.081	2.53	3.88	88.7	...
168	IRAS23060+0505	F23060+0505	230833.97+052129.8	0.1730	...	0.009	0.89	0.61	188.8 ^g	0.71
169	IRAS23129+2548	F23129+2548	231521.41+260432.6	0.1789	...	<0.073	<0.34	0.35	37.2 ^g	0.04
170	IC5298	F23135+2517	231600.67+253324.3	0.0274	...	<0.142	<5.92	7.28	248.9	P+abs

Table 5—Continued

source	Name	FSC Name	J2000 coordinates	z^a	SDSS ^b	EW(6.2 μm) ^c μm	f(6.2 μm) ^d	f(11.3 μm) ^e	$f_\nu(7.7 \mu\text{m})$ mJy	silicate ^f
171	NGC7603	F23163-0001	231856.62+001438.2	0.0295	...	0.018	3.22	5.02	295.7	1.12

^aRedshift from optical redshift in NED unless noted.

^bOur optical classification determined from spectra of the Sloan Digital Sky Survey, determined from presence of broad hydrogen emission lines or ratios among [OIII] λ 5007, H β , [NII] λ 6584, and H α .

^cRest frame equivalent width of 6.2 μm PAH feature fit with single gaussian on a linear continuum within rest wavelength range 5.5 μm to 6.9 μm .

^dTotal flux of PAH 6.2 μm feature fit with single gaussian on a linear continuum within rest wavelength range 5.5 μm to 6.9 μm in units of 10^{-20}W cm^{-2} .

^eTotal flux of PAH 11.3 μm feature fit with single gaussian on a linear continuum within rest wavelength range 10.5 μm to 12 μm in units of 10^{-20}W cm^{-2} .

^fStrength of silicate feature defined as $f_\nu(10 \mu\text{m observed})/f_\nu(10 \mu\text{m continuum})$, for $f_\nu(10 \mu\text{m continuum})$ extrapolated linearly between $f_\nu(7.9 \mu\text{m})$ and $f_\nu(13 \mu\text{m})$. Values > 1 correspond to silicate emission and values < 1 to silicate absorption. Entry P+abs means that both PAH emission and silicate absorption are present; absorption strength is not measured because continuum level at 7.9 μm cannot be reliably determined.

^g $f_\nu(7.9 \mu\text{m})$ measured because continuum peak stronger than $f_\nu(7.7 \mu\text{m})$ at PAH feature.

^hRedshift from IRS spectrum.

ⁱUnique object having optical classification like Blue Compact Dwarf (BCD) with narrow optical emission lines, strong [OIII]/H β and very strong H α /[NII].

Table 6. SEDs and Total Luminosities of AGN

source	FSC Name	$f_{\nu}(25)$ IRS Jy	$f_{\nu}(8)^a$ Jy	$f_{\nu}(12)^b$ Jy	$f_{\nu}(18)^a$ Jy	$f_{\nu}(25)^b$ Jy	$f_{\nu}(60)^b$ Jy	$f_{\nu}(65)^a$ Jy	$f_{\nu}(90)^a$ Jy	$f_{\nu}(100)^b$ Jy	$f_{\nu}(140)^a$ Jy	$f_{\nu}(160)^a$ Jy	$f_{\nu}(1.25)^c$ mJy	$f_{\nu}(1.66)^c$ mJy	R ^d	L_{ir}^e log
1	F00275-2859	0.144	...	0.081	0.137	0.173	0.690	0.352	0.650	0.734	...	1.569	1.31	2.69	4.3 ^f	46.24
2	F00406-3127	0.073	...	0.060	...	0.091	0.717	0.994	7.6 ^f	46.40
3	F00509+1225	0.989	0.321	0.512	0.714	1.210	2.240	1.606	1.964	2.630	2.575	3.055	16.63	25.98	3.68 ^f	45.52
4	F01004-2237	0.538	...	0.227	0.402	0.660	2.290	3.063	1.376	1.790	1.537	...	0.59	0.80	7.05 ^f	45.93
5	F01123-5539	0.333	...	0.213	...	0.417	1.480	2.820	20.37	28.05	4.18	43.83
6	F01199-2307	0.111	...	0.106	...	0.162	1.610	1.698	1.002	1.370	1.298	4.932	17.71 ^f	45.93
7	F01216-3519	0.347	0.141	0.285	0.292	0.449	0.224	0.872	12.08	17.78	3.17	44.03
8	F01348+3254	0.155	...	0.068	...	0.161	0.740	1.164	0.695	1.150	0.257	1.568	2.34	3.08	5.02	46.54
9	F01364-4016	0.121	...	0.174	...	0.166	0.662	0.360	0.672	2.210	1.802	2.928	6.82	8.80	7.21	44.25
10	F01569-2939	0.135	...	0.109	...	0.143	1.730	2.163	1.362	1.510	1.612	0.627	0.54	0.66	13.04 ^f	45.82
11	F01572+0009	0.505	...	0.123	0.244	0.542	2.220	2.014	1.824	2.160	2.943	0.159	3.77	5.96	8.51	46.17
12	F01586-0703	0.347	...	0.187	0.312	0.515	0.511	0.593	11.44	15.76	4.15	43.71
13	F02054+0835	0.162	...	0.177	...	0.234	0.561	0.345	0.645	1.990	0.82	1.06	8.27	46.64
14	F02120-0059	0.265	...	0.192	0.266	0.221	0.489	0.701	0.747	1.460	2.648	...	17.19	22.42	7.85 ^f	44.25
15	F02132-1524	0.167	...	0.111	...	0.226	0.311	0.383	2.37	3.74	9.21 ^f	45.90
16	F02183+0019	0.180	...	0.156	...	0.274	0.411	0.613	4.60	5.30	9.64 ^f	44.86
17	F02191+1313	0.123	...	0.120	...	0.172	0.327	1.670	0.88	1.58	8.81 ^f	45.64
18	F02297-3653	0.368	0.055	0.161	0.265	0.393	1.390	0.863	1.473	2.340	2.876	0.469	12.99	16.90	6.77	44.05
19	F02313+3217	0.213	...	0.083	0.093	0.305	1.690	1.497	1.704	3.490	3.462	3.771	11.65	21.69	6.72	44.03
20	F03158+4227	0.399	...	0.070	...	0.454	4.260	4.101	3.999	4.280	3.796	4.040	12.71 ^f	46.17
21	F03348-3609	1.280	0.342	0.493	0.987	1.430	5.400	4.646	5.972	9.640	10.788	4.447	37.26	47.81	4.61	43.08
22	F03398-2123	0.172	...	0.249	...	0.097	0.601	0.980	0.968	1.490	2.351	1.815	25.64	30.64	3.21 ^f	43.75
23	F03450+0055	0.508	...	0.283	...	0.506	0.471	3.240	10.16	16.35	3.48 ^f	44.62
24	F03538-6432	0.070	...	0.056	...	0.064	0.988	1.022	0.986	1.300	1.543	1.052	0.44	0.80	8.36 ^f	46.35
25	F04213-5620	0.066	...	0.074	...	0.097	0.239	0.519	4.73	7.93	4.53 ^f	44.30
26	F04305+0514	0.617	0.203	0.286	0.497	0.635	1.280	1.314	1.468	2.790	0.476	2.057	13.67	21.16	3.48	44.76
27	F04313-1649	0.056	...	0.066	...	0.071	1.010	0.853	0.814	1.100	1.111	20.96 ^f	46.24
28	F04454-4838	0.417	...	0.090	0.156	0.451	5.680	5.009	4.608	5.250	3.924	2.935	1.17	1.50	18 ^f	45.42
29	F04507+0358	0.599	0.173	0.253	0.471	0.567	0.613	1.137	0.624	1.020	...	1.270	8.91	13.06	2.20	44.48
30	F05136-0012	0.347	0.252	0.319	0.253	0.410	0.643	1.080	24.17	33.69	2.04	44.59
31	F05189-2524	3.058	0.401	0.729	1.685	3.440	13.700	10.407	11.613	11.400	6.907	7.063	9.07	18.46	7.29	45.73
32	F05212-3630	0.168	0.097	0.083	0.216	0.158	0.307	0.787	10.54	13.39	3.02 ^f	44.64
33	F05563-3820	0.619	0.348	0.529	0.536	0.685	0.322	0.559	18.56	32.03	1.51 ^f	44.74
34	F05585-5026	0.096	...	0.100	...	0.081	0.210	1.020	4.17	5.65	4.66 ^f	45.44

Table 6—Continued

source	FSC Name	$f_{\nu}(25)$ IRS Jy	$f_{\nu}(8)^a$ Jy	$f_{\nu}(12)^b$ Jy	$f_{\nu}(18)^a$ Jy	$f_{\nu}(25)^b$ Jy	$f_{\nu}(60)^b$ Jy	$f_{\nu}(65)^a$ Jy	$f_{\nu}(90)^a$ Jy	$f_{\nu}(100)^b$ Jy	$f_{\nu}(140)^a$ Jy	$f_{\nu}(160)^a$ Jy	$f_{\nu}(1.25)^c$ mJy	$f_{\nu}(1.66)^c$ mJy	R ^d	L_{ir}^e log
35	F06035-7102	0.462	0.092	0.116	0.263	0.574	5.130	4.641	4.545	5.650	4.758	3.115	2.03	3.00	7.61	45.79
36	F06206-6315	0.260	...	0.069	0.113	0.294	3.960	3.483	3.526	4.580	4.010	2.179	1.35	1.81	13.35	45.79
37	F06230-6057	0.035	...	0.073	...	0.049	0.159	0.814	4.41	5.31	13.93 ^f	44.21
38	F06279+6342	0.254	0.144	0.168	0.254	0.328	1.430	1.518	1.641	3.120	5.001	3.810	10.62	16.27	5.40	43.83
39	F06361-6217	0.167	...	0.106	...	0.167	1.660	1.449	1.320	2.010	1.745	0.966	0.55	0.68	7.41 ^f	45.99
40	F07260+3955	0.327	...	0.128	...	0.342	0.665	0.536	0.527	0.600	1.29	0.87	8.51 ^f	45.17
41	F07327+5852	0.263	0.176	0.230	0.282	0.390	0.760	0.984	0.795	0.980	0.348	1.427	9.37	14.90	2.38	44.71
42	F07546+3928	0.259	...	0.140	...	0.276	0.173	0.716	10.94	16.02	2.30	45.24
43	F07588+4651	0.141	...	0.126	...	0.147	0.270	1.010	1.35	1.44	5.04	45.42
44	F07599+6508	0.475	0.245	0.264	0.370	0.535	1.690	1.102	1.299	1.730	1.501	1.526	9.50	20.19	3.03	46.09
45	F08216+3009	0.277	0.121	0.193	...	0.401	0.421	0.630	3.64	6.07	2.65	44.21
46	F08520-6850	0.613	0.109	0.124	0.299	0.658	5.260	5.003	4.974	5.980	4.905	3.251	1.47	2.03	5.04 ^f	45.30
47	F08572+3915	1.559	0.312	0.318	0.794	1.700	7.430	5.927	5.134	4.590	2.618	1.431	0.74	0.97	2.85 ^f	45.71
48	F09155+5541	0.083	...	0.066	...	0.128	0.199	0.512	2.19	2.85	4.68	44.40
49	F09182-0750	0.351	...	0.080	0.263	0.381	0.654	1.100	3.46	4.84	4.95	43.94
50	F09233+1257	0.245	0.099	0.154	0.214	0.215	0.590	0.962	0.926	0.918	0.051	3.677	11.44	14.49	3.18	44.28
51	F09320+6134	0.830	0.135	0.250	0.457	1.030	11.500	11.183	14.555	20.200	15.550	11.571	6.39	12.77	9.67	45.56
52	F09414+4843	0.129	...	0.134	...	0.188	0.556	0.233	0.545	0.808	1.298	...	1.58	2.07	4.92	44.79
53	F09589+2901	0.279	0.112	0.160	0.274	0.258	0.231	0.344	1.17	2.10	2.33	45.84
54	F10038-3338	0.970	0.323	0.294	0.371	1.110	8.900	8.164	8.762	7.980	4.990	4.264	3.14	8.13	2.36 ^f	45.27
55	F10036+4136	0.090	...	0.126	...	0.115	0.273	0.559	1.73	2.26	7.32	45.55
56	F10111-3544	0.259	...	0.132	0.307	0.211	0.514	1.020	4.95	6.79	6.01	44.22
57	F10156+6413	0.174	...	0.128	...	0.162	0.741	1.840	5.70	6.71	4.91	44.64
58	F10207+2007	1.520	0.444	0.667	1.128	1.760	7.820	7.112	10.596	17.600	17.171	11.387	49.72	62.97	5.34	43.51
59	F10378+1108	0.177	...	0.114	...	0.235	2.280	2.017	2.131	1.820	1.464	0.754	0.93	1.28	15.86 ^f	45.93
60	F10459-2453	0.577	...	0.131	0.424	0.753	2.250	1.510	2.089	3.870	2.750	2.591	16.78	21.34	10.32	43.97
61	F10590+6515	0.201	...	0.068	...	0.217	0.541	0.953	2.58	3.54	4.39	45.04
62	F11095-0238	0.358	...	0.135	...	0.418	3.250	2.552	2.929	2.530	1.472	...	0.56	0.68	6.52 ^f	45.86
63	F11119+3257	0.337	0.087	0.167	0.246	0.348	1.590	2.016	1.727	1.520	0.352	0.712	3.73	7.04	4.38 ^f	46.20
64	F11233+3451	0.167	...	0.114	...	0.213	0.561	0.318	0.587	1.060	0.549	0.454	1.57	2.70	3.99	45.43
65	F11330+5713	0.476	0.114	0.133	0.343	0.501	1.670	1.668	1.733	2.150	3.442	0.594	6.32	10.38	3.63	45.05
66	F11365-3727	1.972	0.502	0.840	1.530	2.490	3.260	2.634	2.716	4.900	3.469	5.855	25.64	39.87	4.33	44.26
67	F11431-1810	0.128	...	0.116	...	0.120	0.228	0.679	6.48	7.94	3.56	44.17
68	F11486-2019	0.128	...	0.099	...	0.153	0.629	0.285	0.483	0.580	0.45	0.50	35.75 ^f	43.38

Table 6—Continued

source	FSC Name	$f_{\nu}(25)$ IRS Jy	$f_{\nu}(8)^a$ Jy	$f_{\nu}(12)^b$ Jy	$f_{\nu}(18)^a$ Jy	$f_{\nu}(25)^b$ Jy	$f_{\nu}(60)^b$ Jy	$f_{\nu}(65)^a$ Jy	$f_{\nu}(90)^a$ Jy	$f_{\nu}(100)^b$ Jy	$f_{\nu}(140)^a$ Jy	$f_{\nu}(160)^a$ Jy	$f_{\nu}(1.25)^c$ mJy	$f_{\nu}(1.66)^c$ mJy	R ^d	L_{ir}^e log
69	F11500-0211	0.101	...	0.079	...	0.131	0.944	0.078	0.799	0.896	0.500	43.82 ^g	42.38
70	F11513+6155	0.132	...	0.088	...	0.147	0.279	1.320	0.83	1.16	5.21 ^f	45.58
71	F11583+0705	0.116	...	0.132	...	0.144	0.375	0.752	4.83	6.11	3.74	44.34
72	F12021+3126	0.324	...	0.170	0.186	0.379	2.750	5.570	9.46	11.03	9.47	44.62
73	F12072-0444	0.458	...	0.119	0.252	0.537	2.460	1.772	2.319	2.470	0.756	1.796	1.08	1.42	9.72 ^f	45.97
74	...	4.375	1.032	2.010	3.629	4.870	6.460	4.754	4.594	8.880	5.520	5.505	125.22	172.15	3.04	43.52
75	F12127-1412	0.207	...	0.125	...	0.245	1.540	0.956	1.281	1.130	1.622	1.328	0.46	1.17	5.95 ^f	45.79
76	F12329-3938	1.502	0.510	0.457	1.163	1.390	4.310	3.738	4.370	5.400	5.391	3.265	22.75	30.73	3.31	44.21
77	F12362-2702	0.280	0.114	0.148	0.207	0.268	0.498	0.102	0.613	0.831	9.25	14.08	1.71 ^f	44.13
78	F12440+0238	0.110	...	0.161	...	0.156	0.271	0.424	1.87	2.51	6.99	44.58
79	F12464-0053	0.193	...	0.164	...	0.273	0.242	0.434	1.93	2.39	10.97 ^f	45.19
80	F12505-0256	0.397	...	0.175	0.298	0.490	0.618	0.638	0.9	0.74	7.62 ^f	44.16
81	F12514+1027	0.128	...	0.063	...	0.190	0.712	0.688	0.788	0.755	...	0.991	0.41	0.85	4.02 ^f	46.36
82	F12540+5708	7.399	1.051	1.870	4.396	8.660	32.000	31.194	28.610	30.300	19.518	15.524	42.86	94.51	5169 ^f	46.11
83	F13016-0517	0.338	...	0.390	...	0.460	1.870	4.790	19.15	23.31	19.54	42.96
84	F13036-4008	1.233	0.472	0.683	0.902	1.220	5.660	5.453	6.945	8.790	7.792	6.404	39.67	64.79	3.24	44.53
85	F13197-1627	2.513	0.453	0.878	1.873	2.860	5.890	4.537	4.634	5.480	4.384	1.328	18.45	24.16	4.02	44.70
86	F13218+0552	0.305	0.216	0.262	0.328	0.403	1.170	1.216	0.892	0.713	0.80	2.12	1.98 ^f	46.26
87	F13279+3402	0.106	...	0.094	...	0.126	1.180	1.043	0.822	1.200	0.160	0.033	2.02	2.27	12.22 ^f	44.04
88	F13330-3402	0.762	...	0.380	...	0.809	1.090	1.100	2.68 ^f	43.49
89	F13342+3932	0.198	...	0.119	...	0.253	1.110	1.378	1.034	1.630	2.582	2.737	1.77	2.94	6.52	46.03
90	F13352+6402	0.055	...	0.056	...	0.078	0.987	0.710	0.966	1.430	1.456	0.489	0.31	0.39	7.27	46.14
91	F13349+2438	0.758	0.449	0.631	0.612	0.841	0.611	0.990	12.21	19.89	1.8 ^f	45.88
92	F13428+5608	1.979	0.135	0.235	0.871	2.280	21.700	22.542	20.232	21.400	14.278	12.111	7.01	10.14	13.13	45.72
93	F13450+6437	0.055	...	0.052	...	0.065	0.158	0.641	4.67	5.37	10.48	43.68
94	F13451+1232	0.523	...	0.143	0.311	0.669	1.920	1.899	1.748	2.060	0.959	0.971	1.70	2.16	11.45	45.90
95	F13464-3003	2.137	0.769	1.080	1.790	2.210	2.030	1.811	1.785	1.660	1.565	2.705	47.78	74.52	1.91	44.52
96	F13510+3344	0.830	0.138	0.308	0.601	0.962	1.420	1.065	1.215	2.640	3.359	1.616	11.99	14.20	5.19	43.56
97	F13536+1836	1.455	0.376	0.510	1.103	1.580	2.180	2.004	1.584	1.920	2.207	1.907	5.25	14.73	2.66	45.36
98	F14026+4341	0.223	...	0.118	0.254	0.285	0.622	0.994	3.33	4.75	6.27 ^f	46.49
99	F14029+2610	0.113	...	0.130	...	0.124	0.230	0.699	2.74	4.56	3.87 ^f	45.65
100	F14036+4040	0.204	...	0.065	...	0.191	0.265	0.382	1.46	1.47	3.78	44.90
101	F14047+2841	0.429	0.080	0.185	0.305	0.399	0.729	0.938	4.54	6.44	3.78	45.25
102	F14106-0258	3.296	0.823	1.280	2.240	3.640	8.410	7.528	8.413	8.890	7.723	5.429	23.64	68.66	2.60	43.99

Table 6—Continued

source	FSC Name	$f_{\nu}(25)$ IRS Jy	$f_{\nu}(8)^a$ Jy	$f_{\nu}(12)^b$ Jy	$f_{\nu}(18)^a$ Jy	$f_{\nu}(25)^b$ Jy	$f_{\nu}(60)^b$ Jy	$f_{\nu}(65)^a$ Jy	$f_{\nu}(90)^a$ Jy	$f_{\nu}(100)^b$ Jy	$f_{\nu}(140)^a$ Jy	$f_{\nu}(160)^a$ Jy	$f_{\nu}(1.25)^c$ mJy	$f_{\nu}(1.66)^c$ mJy	R ^d	L_{ir}^e log
103	F14157+2522	0.587	0.157	0.401	0.409	0.769	1.070	0.476	1.073	1.610	2.552	...	31.02	45.87	4.78	44.20
104	F14164-2625	0.081	...	0.161	...	0.120	0.466	0.587	0.847	1.770	2.148	3.978	11.12	16.21	6.15 ^f	44.05
105	F14180+5437	0.108	...	0.066	...	0.086	0.212	0.546	10.15	13.02	2.7 ^f	45.40
106	F14265+0130	0.197	...	0.133	0.139	0.208	0.236	0.379	9.70	14.12	2.59	45.08
107	F14348-1447	0.403	...	0.140	...	0.495	6.870	6.633	8.363	7.070	5.275	3.312	1.55	2.24	15.95	45.92
108	F14376+0300	0.139	...	0.112	...	0.159	0.303	0.428	0.82	0.70	14.05 ^f	44.09
109	F14390+5343	0.521	...	0.126	...	0.509	1.310	1.850	3.98	5.04	5.15	44.73
110	F14400+3539	0.191	...	0.121	...	0.187	0.570	0.588	0.648	0.924	0.897	0.069	10.67	16.21	3.15	45.11
111	F14396-1702	0.702	0.176	0.243	0.418	0.882	8.160	7.135	11.383	14.700	11.847	10.322	17.11	22.10	8.67	44.17
112	F14463+3612	0.089	...	0.066	...	0.133	0.245	0.525	1.86	2.72	7.05	45.17
113	F14474+4233	0.221	0.093	0.114	0.162	0.234	0.403	0.555	0.82	1.45	2.95	45.80
114	F14541+4906	0.201	...	0.083	0.125	0.200	0.530	0.543	0.33	0.63	4.89 ^f	46.07
115	F14589+2340	0.055	...	0.065	...	0.085	0.195	0.515	0.64	1.32	7.75 ^f	45.88
116	F15034+0353	0.208	...	0.129	...	0.196	0.381	0.903	5.99	8.69	4.35	44.38
117	F15065+0446	0.105	...	0.057	...	0.119	0.338	0.768	0.86	1.19	5.24	45.21
118	F15146+1911	0.147	0.102	0.139	...	0.121	0.200	0.757	6.72	9.23	2.27 ^f	45.80
119	F15176+5216	0.228	...	0.079	0.182	0.279	0.780	0.520	0.803	1.340	1.473	1.596	1.99	3.61	4.30	45.70
120	F15225+2350	0.151	...	0.069	...	0.180	1.300	0.951	1.109	1.480	1.904	1.863	0.62	0.94	8.52 ^f	45.75
121	F15250+3608	1.107	0.098	0.200	0.452	1.320	7.290	6.757	5.520	5.910	3.945	2.383	2.45	3.20	7.06 ^f	45.62
122	F15295+2414	0.319	...	0.120	0.186	0.333	0.985	0.529	0.905	0.952	0.836	1.873	4.06	4.76	5.86	45.42
123	F15390+5619	0.117	...	0.058	...	0.116	0.460	0.524	1.84	1.80	3.60	44.84
124	F15439+4855	0.103	...	0.074	...	0.108	0.283	0.447	1.34	1.97	4.42 ^f	46.38
125	F15456+5506	0.152	...	0.084	...	0.155	0.198	0.605	0.96	1.55	2.52	45.18
126	F16094+4902	0.096	...	0.078	...	0.125	0.213	0.393	2.21	2.68	6.13	44.33
127	F16090-0139	0.230	...	0.090	...	0.264	3.610	2.491	3.248	4.870	4.443	4.303	1.04	1.37	9.35 ^f	46.12
128	F16136+6550	0.212	0.082	0.097	0.178	0.237	0.597	0.549	0.541	0.810	0.855	0.193	8.64	10.45	3.06	45.55
129	F16121+2611	0.100	...	0.089	...	0.139	0.191	0.413	3.00	4.29	4.24	45.32
130	F16149+3723	0.106	...	0.056	...	0.104	0.181	0.526	1.14	1.46	6.07	45.37
131	F16328+2055	0.127	...	0.085	...	0.141	0.559	0.239	0.579	1.170	1.468	...	2.20	4.28	4.81	45.51
132	F16463+3027	0.161	...	0.087	...	0.170	0.200	0.520	1.58	2.07	3.62	45.14
133	F16574+1838	0.155	...	0.119	...	0.163	0.277	0.853	1.49	2.31	4.00	45.72
134	F17002+5153	0.200	0.069	0.104	0.127	0.235	0.384	0.969	4.75	6.37	3.26 ^f	46.29
135	F17044+6720	0.313	...	0.068	0.182	0.357	1.280	1.262	0.986	0.978	1.235	0.585	0.66	1.00	5.35 ^f	45.75
136	F17040+6048	0.110	...	0.070	...	0.128	0.296	0.697	3.49	4.18	5.63	46.36

Table 6—Continued

source	FSC Name	$f_\nu(25)$ IRS Jy	$f_\nu(8)$ ^a Jy	$f_\nu(12)$ ^b Jy	$f_\nu(18)$ ^a Jy	$f_\nu(25)$ ^b Jy	$f_\nu(60)$ ^b Jy	$f_\nu(65)$ ^a Jy	$f_\nu(90)$ ^a Jy	$f_\nu(100)$ ^b Jy	$f_\nu(140)$ ^a Jy	$f_\nu(160)$ ^a Jy	$f_\nu(1.25)$ ^c mJy	$f_\nu(1.66)$ ^c mJy	R ^d	L_{ir} ^e log
137	F17068+4027	0.128	...	0.076	...	0.122	1.330	1.424	1.044	1.410	1.835	0.984	0.38	0.50	7.38 ^f	45.98
138	F17130+5733	0.139	...	0.053	...	0.120	0.156	0.540	1.16	1.47	3.37	45.09
139	F17341+5704 ^h	0.129	...	0.095	...	0.138	0.198	0.480	0.51	0.32	11.04	44.43
140	F18072+6948	0.172	0.084	0.103	0.122	0.181	0.270	0.702	14.01	18.93	2.34 ^f	44.59
141	F18216+6419A	0.454	0.131	0.211	0.326	0.498	1.440	0.692	0.635	2.740	0.465	...	11.90	14.73	4.48	46.72
142	F18332+3239	0.119	0.120	0.095	...	0.106	0.182	0.773	16.80	24.56	1.63 ^f	44.62
143	F18325-5926	1.257	...	0.623	...	1.380	3.230	3.900	24.94	47.37	2.88	44.64
144	F18333-6528	2.053	0.300	0.612	1.446	2.360	2.310	1.833	1.227	1.050	1.828	...	9.92	14.56	3.27	44.27
145	F18456+7943	0.232	0.090	0.128	0.242	0.287	0.204	0.617	5.80	9.37	3.18	44.74
146	F18443+7433	0.182	...	0.096	...	0.200	2.110	1.897	1.545	2.280	1.594	1.827	9.61 ^f	45.90
147	F18402-6224	0.928	0.301	0.467	0.697	1.030	1.840	1.838	1.705	2.750	2.621	1.635	18.52	31.76	3.04	44.17
148	F18389-7834	0.125	...	0.090	...	0.180	0.373	1.200	6.45	8.45	5.57 ^f	44.99
149	F19169-5845	0.311	0.150	0.242	0.233	0.352	0.575	1.480	13.67	20.02	3.19 ^f	44.64
150	F19254-7245	1.201	0.149	0.221	0.658	1.240	5.480	5.570	4.809	5.790	5.183	4.719	3.64	5.04	16.42 ^f	45.66
151	F20036-1547	0.215	...	0.125	...	0.281	1.650	0.620	1.705	1.980	2.561	0.777	2.68	4.70	16.52	46.20
152	F20045-6114	0.238	0.155	0.250	0.357	0.310	0.960	0.555	1.369	2.190	3.756	3.846	19.81	28.94	2.78	43.92
153	F20100-4156	0.348	...	0.135	...	0.343	5.230	4.289	4.648	5.160	4.214	3.562	13.43 ^f	46.21
154	F20210+1121	1.260	0.172	0.295	0.846	1.400	3.380	2.602	2.522	2.680	2.943	0.345	3.35	3.93	6.06	45.46
155	F20414-1054	0.641	0.247	0.316	0.499	0.702	1.360	1.520	25.24	36.43	2.69	44.78
156	F20460+1925	0.525	0.178	0.229	0.333	0.528	0.883	1.450	2.96	5.91	2.57	46.15
157	F20482-5715	3.096	...	1.070	2.246	3.910	5.340	4.745	3.821	4.170	4.016	0.155	16.69	22.49	4.55	44.42
158	F20551-4250	1.521	0.131	0.284	0.716	1.910	12.800	12.493	11.119	9.950	7.004	3.954	4.27	5.43	9.52 ^f	45.62
159	F21382-4032	0.064	...	0.063	...	0.095	0.184	0.566	0.76	0.86	17.02 ^f	44.51
160	F21523-0936	0.192	...	0.136	...	0.195	0.329	0.858	6.46	8.05	2.94 ^f	45.88
161	F21591-3206	0.501	0.316	0.437	0.424	0.761	5.710	4.856	8.087	12.300	11.631	12.947	15.85	25.39	4.30	44.03
162	F22006+4202	0.323	0.247	0.139	0.319	0.250	0.403	0.150	0.937	1.970	1.335	1.144	20.99	31.07	1.91 ^f	45.08
163	F22045+0959	0.548	...	0.196	...	0.769	2.880	4.890	7.28	8.54	9.16	44.72
164	F22061-4724	0.508	0.360	0.606	...	0.742	2.670	1.516	2.943	8.180	8.316	7.604	69.07	120.20	10.96 ^f	43.55
165	F22212-0221	0.296	0.141	0.208	0.358	0.264	0.306	1.030	7.35	12.67	2.53 ^f	44.88
166	F22341-1248	0.252	...	0.175	0.482	0.354	0.458	0.511	0.511	1.010	2.017	...	7.18	10.22	6.75	44.16
167	F22377+0747	0.273	...	0.203	0.141	0.344	0.826	0.761	0.873	2.480	0.025	0.916	10.33	13.03	4.87	44.35
168	F23060+0505	0.490	0.160	0.198	0.378	0.426	1.150	1.285	1.175	0.833	1.510	0.012	2.38	5.62	2.55 ^f	46.07
169	F23129+2548	0.094	...	0.075	...	0.131	1.810	1.306	1.453	1.640	0.643	1.284	0.59	0.68	12.01 ^f	46.07
170	F23135+2517	1.421	0.177	0.262	0.749	1.800	9.760	6.997	10.206	11.100	9.004	7.182	10.68	16.20	9.36	45.16

Table 6—Continued

source	FSC Name	$f_\nu(25)$ IRS Jy	$f_\nu(8)^a$ Jy	$f_\nu(12)^b$ Jy	$f_\nu(18)^a$ Jy	$f_\nu(25)^b$ Jy	$f_\nu(60)^b$ Jy	$f_\nu(65)^a$ Jy	$f_\nu(90)^a$ Jy	$f_\nu(100)^b$ Jy	$f_\nu(140)^a$ Jy	$f_\nu(160)^a$ Jy	$f_\nu(1.25)^c$ mJy	$f_\nu(1.66)^c$ mJy	R ^d	L_{ir}^e log
171	F23163-0001	0.336	0.295	0.158	0.321	0.241	0.853	1.144	1.340	2.040	2.419	1.330	25.19	34.32	1.23	44.42

^aFlux densities at listed wavelengths taken from AKARI catalog, <http://darts.isas.jaxa.jp/astro/akari/cas/tools/search/crossid.html>.

^bFlux densities at listed wavelengths taken from IRAS Faint Source Catalog, <http://vizier.u-strasbg.fr/viz-bin/VizieR-4>.

^cFlux densities at listed wavelengths taken from 2MASS catalog.

^dRatio $R = f_{IR}/\nu f_\nu(7.7 \text{ or } 7.9 \mu\text{m})$, for $f_{IR} = 1.8 \times 10^{-11}[13.48f_\nu(12) + 5.16f_\nu(25) + 2.58f_\nu(60) + f_\nu(100)]$ in $\text{erg cm}^{-2} \text{ s}^{-1}$.

^eTotal infrared luminosity $L_{ir} = 4\pi D^2 f_{IR}$ in erg s^{-1} for D the luminosity distance determined for $H_0 = 71 \text{ km s}^{-1} \text{ Mpc}^{-1}$, $\Omega_M=0.27$ and $\Omega_\Lambda=0.73$, from Wright (2006): <http://www.astro.ucla.edu/~wright/CosmoCalc.html>.

^f $f_\nu(7.9 \mu\text{m})$ measured because continuum peak stronger than $f_\nu(7.7 \mu\text{m})$ at PAH feature.

^gUnique object, having highest value of R accompanied by unusually low L_{ir} ; no SDSS spectrum but optical image resembles BCD.

^hUnique object noted in Table 5 with weak PAH and optical spectrum like low luminosity BCD (e.g. Hunt et al. 2010), but L_{ir} compares to normal starbursts and AGN.

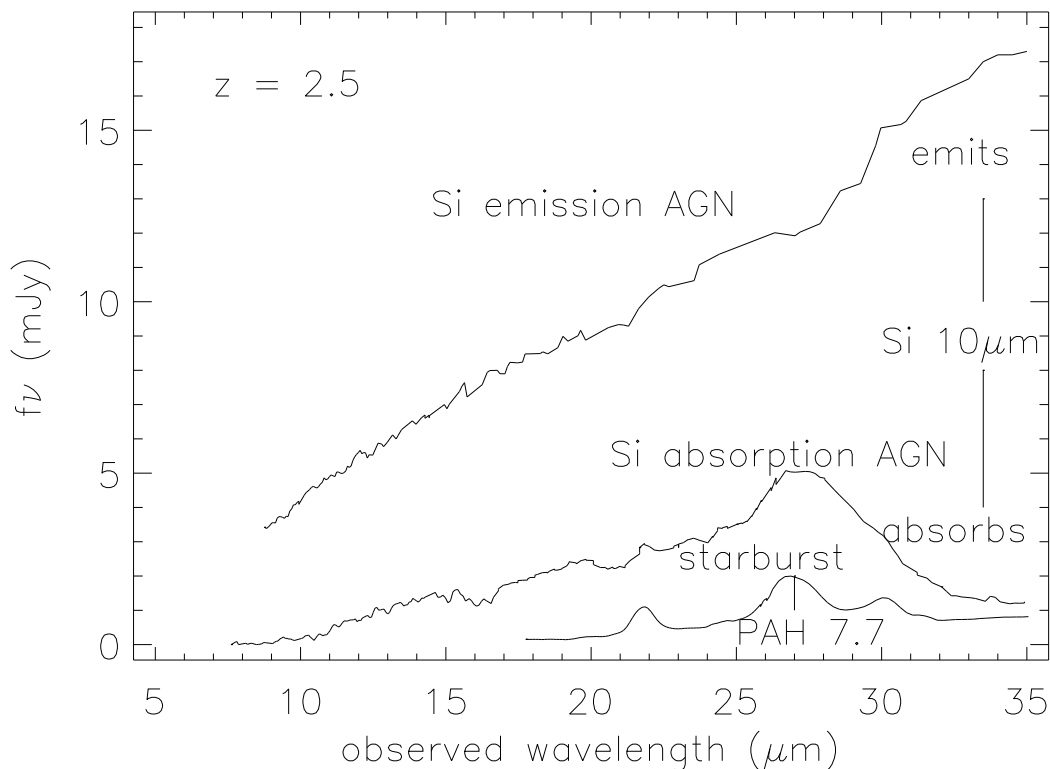


Fig. 1.— Representative spectra of AGN and starbursts as would be observed at $z = 2.5$. Spectra indicate why the parameter νf_ν ($\sim 8 \mu\text{m}$) (rest frame) is used because it is a straightforward measurement of the spectral peak in high redshift sources with poor S/N. Flux densities represent the brightest sources known in each category at this redshift.

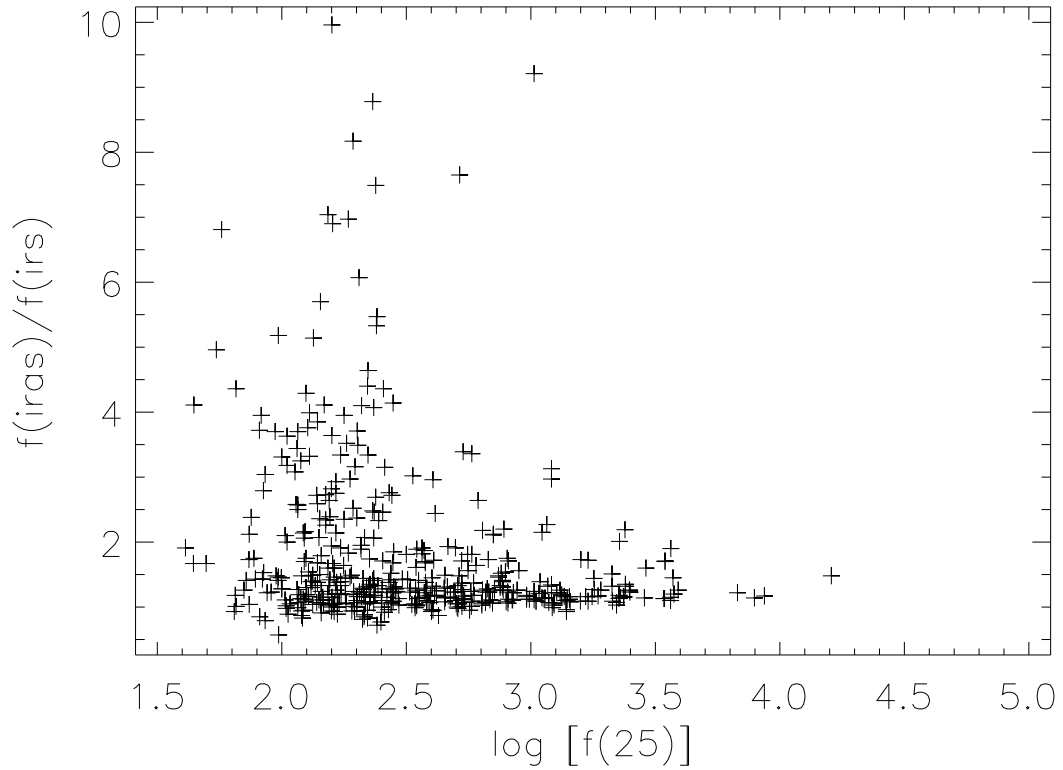


Fig. 2.— Ratio of actual $f_\nu(25 \mu\text{m})$ observed with IRAS, $f(\text{IRAS})$, to synthetic $f_\nu(25 \mu\text{m})$ measured on IRS spectrum, $f(\text{IRS})$, compared to IRAS $f_\nu(25 \mu\text{m})$ in mJy. If ratio ~ 1 , it means that source is unresolved with the $10''$ IRS LL1 slit so that IRAS and IRS measure the same source. Larger ratios correspond to more extended sources. Using these results, we study in this paper only those sources for which $f(\text{IRAS})/f(\text{IRS}) < 1.5$.

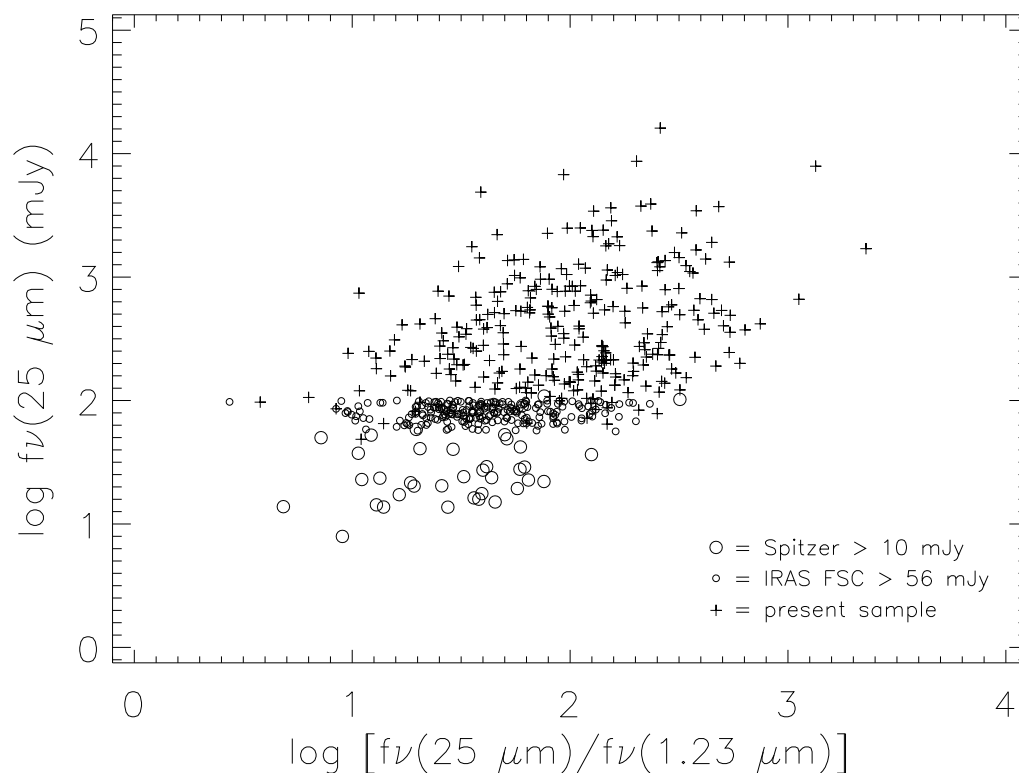


Fig. 3.— Range of ratios of mid-infrared (from dust) measured as IRAS $f_\nu(25 \mu\text{m})$ to near-infrared (from stars or non-thermal AGN continuum) measured as 2MASS J band flux density. Crosses are the sources from our present sample in Tables 1-6; small circles are all IRAS Faint Source Catalog sources with $56 \text{ mJy} < f_\nu(25 \mu\text{m}) < 100 \text{ mJy}$, the faintest FSC sample (Hovhannisyan et al. 2010); large circles are the *Spitzer* flux limited sample with $f_\nu(24 \mu\text{m}) > 10 \text{ mJy}$ from Weedman and Houck (2009a).

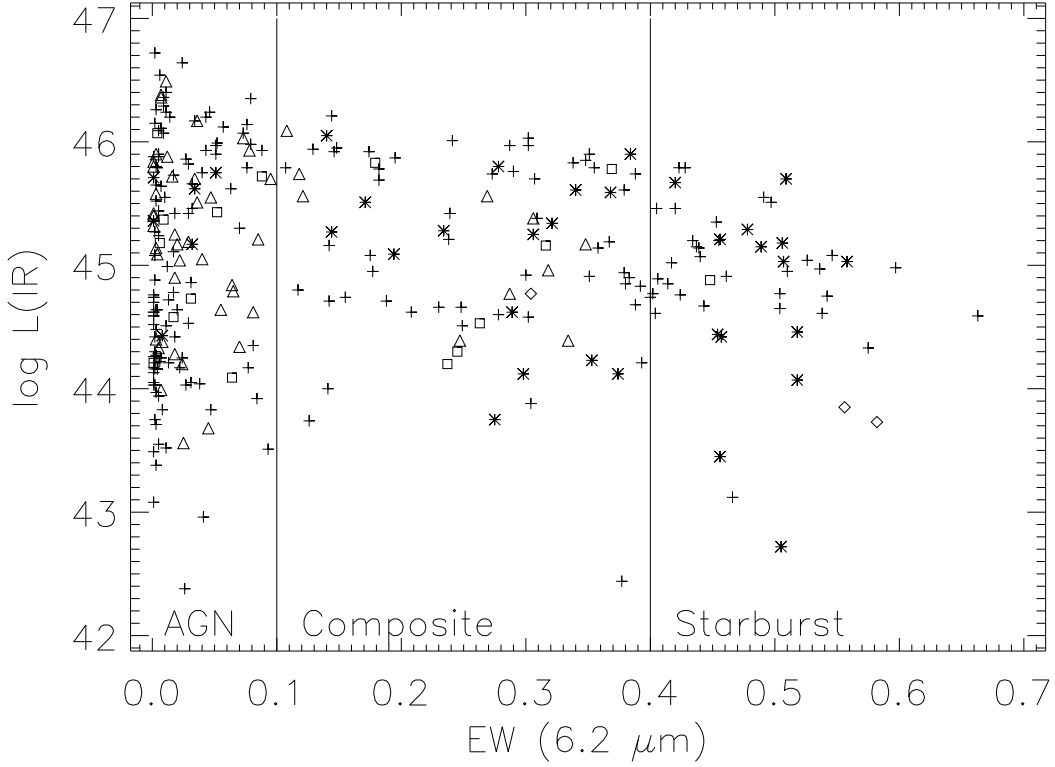


Fig. 4.— Infrared luminosity L_{IR} in erg s^{-1} measured from total IRAS flux compared to equivalent width of $6.2 \mu\text{m}$ PAH feature, in μm . Symbols indicate optical classification if available from SDSS spectra, determined from presence of broad hydrogen emission lines or ratios among $[\text{OIII}] \lambda 5007$, $\text{H}\beta$, $[\text{NII}] \lambda 6584$, and $\text{H}\alpha$; triangles are optically classified AGN, squares are optically classified composite sources, asterisks are optically classified starbursts, and diamonds are absorption line sources not classifiable with emission lines; crosses are sources without SDSS spectra available for optical classification. Vertical lines divide sources classified according to infrared classification from $\text{EW}(6.2 \mu\text{m})$, with "pure" AGN defined by $\text{EW}(6.2 \mu\text{m}) < 0.1 \mu\text{m}$, "pure" starbursts, defined as $\text{EW}(6.2 \mu\text{m}) > 0.4 \mu\text{m}$, and composite starburst+AGN defined as $0.1 \mu\text{m} < \text{EW}(6.2 \mu\text{m}) < 0.4 \mu\text{m}$.

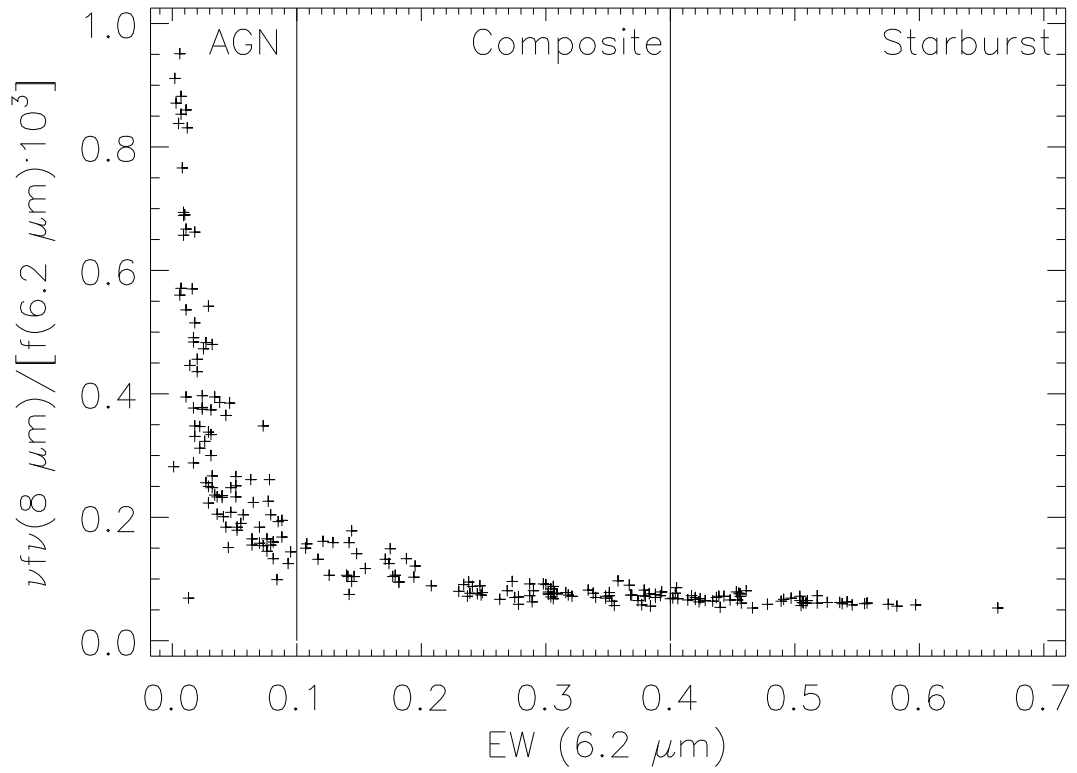


Fig. 5.— Comparison of peak flux $\nu f_{\nu}(\sim 8 \mu\text{m})$ with total flux measured in PAH $6.2 \mu\text{m}$ feature. The peak flux is the peak of the $7.7 \mu\text{m}$ PAH feature if this feature is the local spectral maximum; for AGN without PAH features, the peak is the continuum at $7.9 \mu\text{m}$.

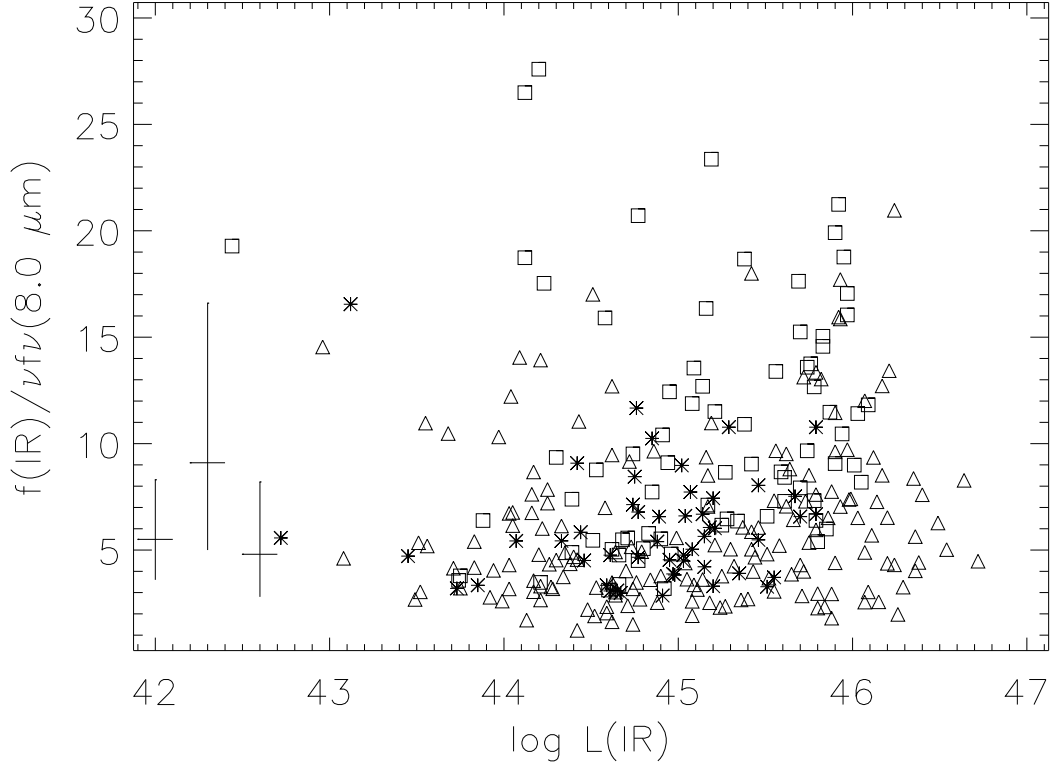


Fig. 6.— Ratio $f_{IR}/\nu f_\nu(\sim 8 \mu\text{m})$ for all sources compared to infrared luminosity L_{IR} in erg s^{-1} measured from total IRAS flux. Asterisks are starbursts, defined as sources with $\text{EW}(6.2 \mu\text{m}) > 0.4 \mu\text{m}$ for which spectral peak is the $7.7 \mu\text{m}$ PAH feature; squares are composite sources with $0.1 \mu\text{m} < \text{EW}(6.2 \mu\text{m}) < 0.4 \mu\text{m}$ for which spectral peak is usually the $7.7 \mu\text{m}$ PAH feature except for sources noted in Table 3 for which continuum peak at $7.9 \mu\text{m}$ is stronger than PAH peak; triangles are AGN for which spectral peak is either the $7.7 \mu\text{m}$ PAH feature or the $7.9 \mu\text{m}$ continuum as noted in Table 5. Error bars show medians and dispersions for starbursts, composites, and AGN (left to right).

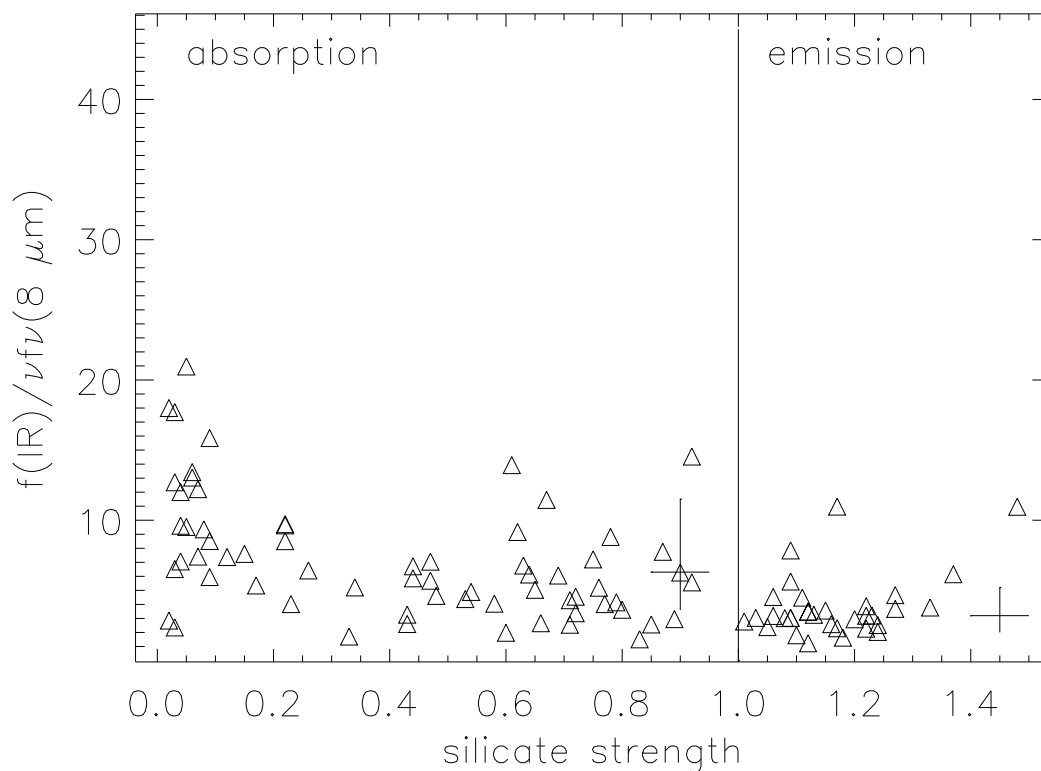


Fig. 7.— Ratio $f_{IR}/\nu f_{\nu}(\sim 8 \mu\text{m})$ for AGN sources compared to strength of silicate feature. Strength of feature is defined as $f_{\nu}(10 \mu\text{m observed})/f_{\nu}(10 \mu\text{m continuum})$, for $f_{\nu}(10 \mu\text{m continuum})$ extrapolated linearly between $f_{\nu}(7.9 \mu\text{m})$ and $f_{\nu}(13 \mu\text{m})$. Values > 1 correspond to silicate emission and values < 1 to silicate absorption. Error bars show medians and dispersions for absorption and emission AGN.

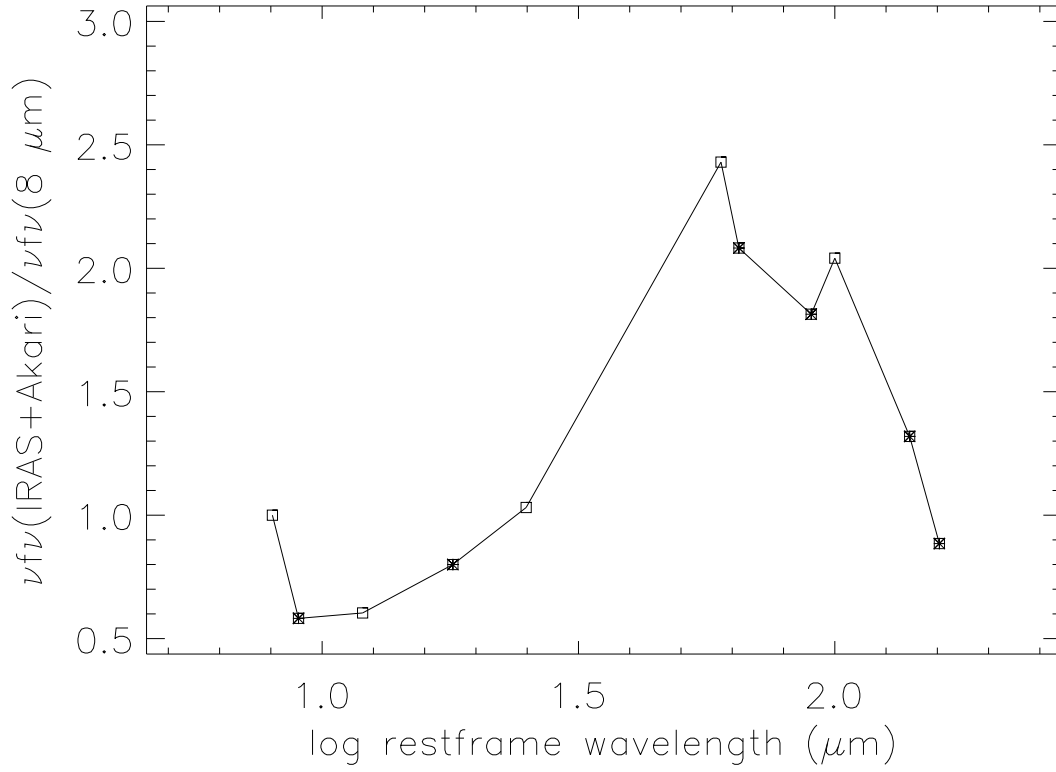


Fig. 8.— Median spectral energy distribution in the rest frame normalized to the peak $\nu f_\nu(\sim 8 \mu\text{m})$ for all 190 sources having both IRAS (open squares) and complete AKARI (filled squares) flux densities. AGN, composites, and starbursts are all combined in this plot.

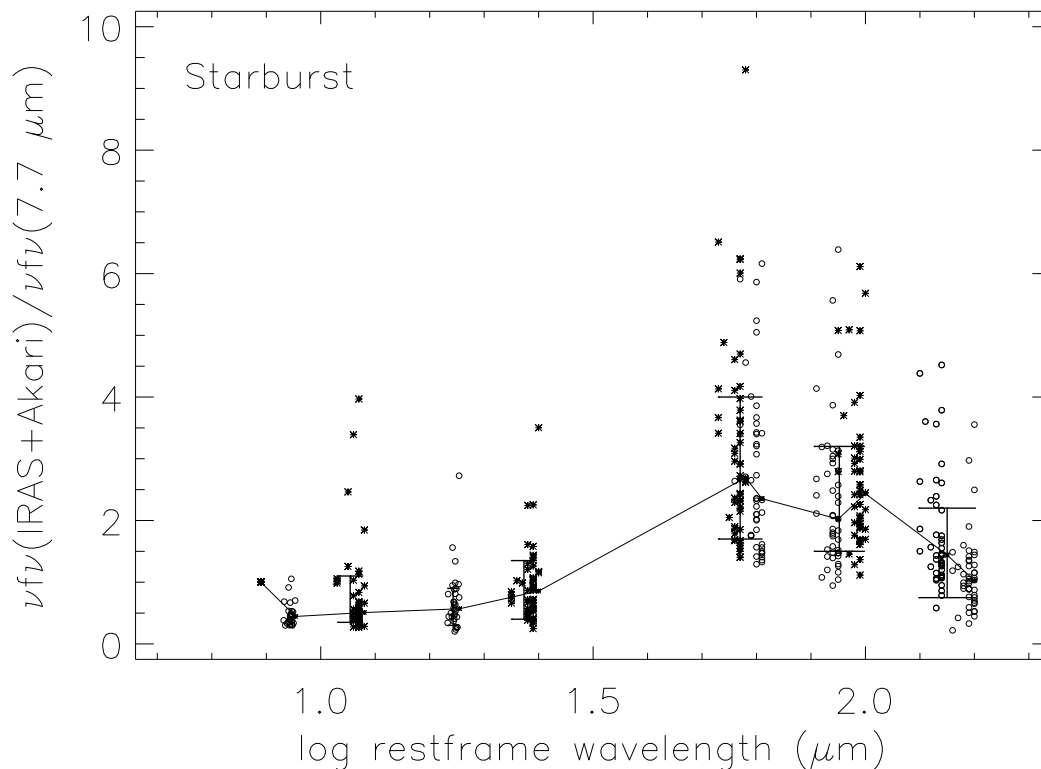


Fig. 9.— Spectral energy distributions for all starburst sources as determined from IRAS and AKARI flux densities, in the rest frame normalized to the peak $\nu f_{\nu}(7.7 \mu\text{m})$. Solid line shows medians at the observing wavelengths. Asterisks are flux densities from IRAS, and circles are from AKARI. Observed points are at rest frame wavelengths and are distributed in wavelength because of different source redshifts. Error bars show one σ dispersions at the various rest frame wavelengths; dispersions are determined using combined points for $60 \mu\text{m}$ and $65 \mu\text{m}$, for $90 \mu\text{m}$ and $100 \mu\text{m}$, and for $140 \mu\text{m}$ and $160 \mu\text{m}$.

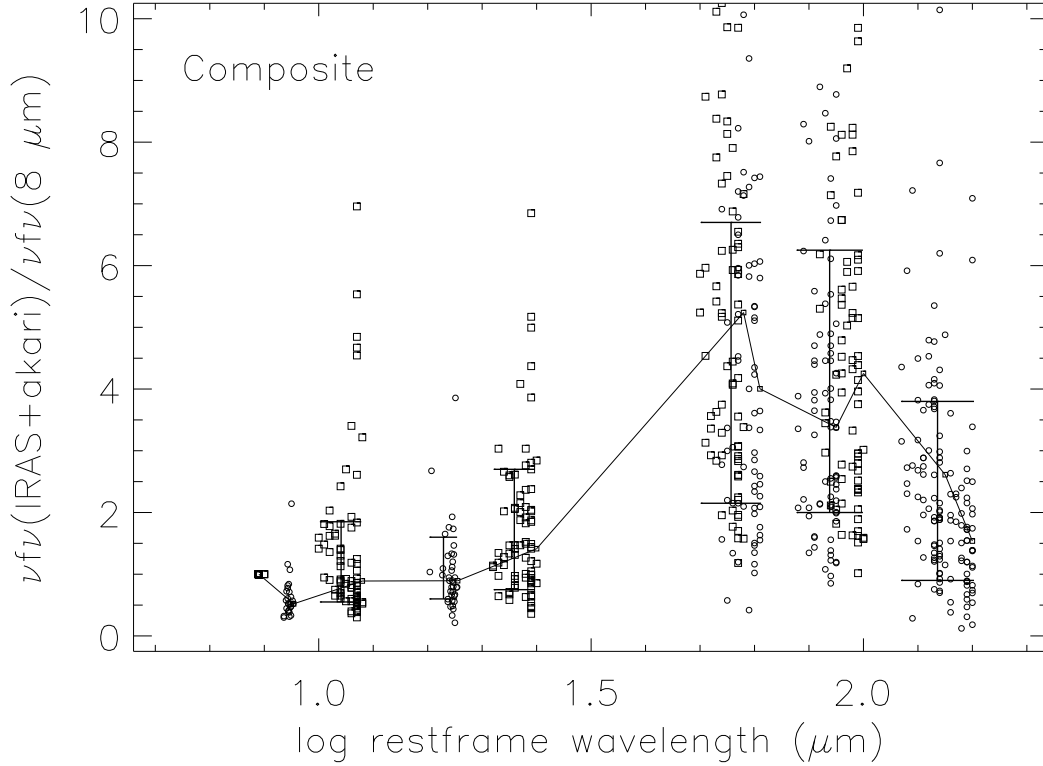


Fig. 10.— Spectral energy distributions for all composite sources as determined from IRAS and AKARI flux densities, in the rest frame normalized to the peak $\nu f_{\nu}(\sim 8 \mu\text{m})$. Solid line shows medians at the observing wavelengths. Squares are flux densities from IRAS, and circles are from AKARI. Observed points are at rest frame wavelengths and are distributed in wavelength because of different source redshifts. Error bars show one σ dispersions at the various rest frame wavelengths; dispersions are determined using combined points for $60 \mu\text{m}$ and $65 \mu\text{m}$, for $90 \mu\text{m}$ and $100 \mu\text{m}$, and for $140 \mu\text{m}$ and $160 \mu\text{m}$.

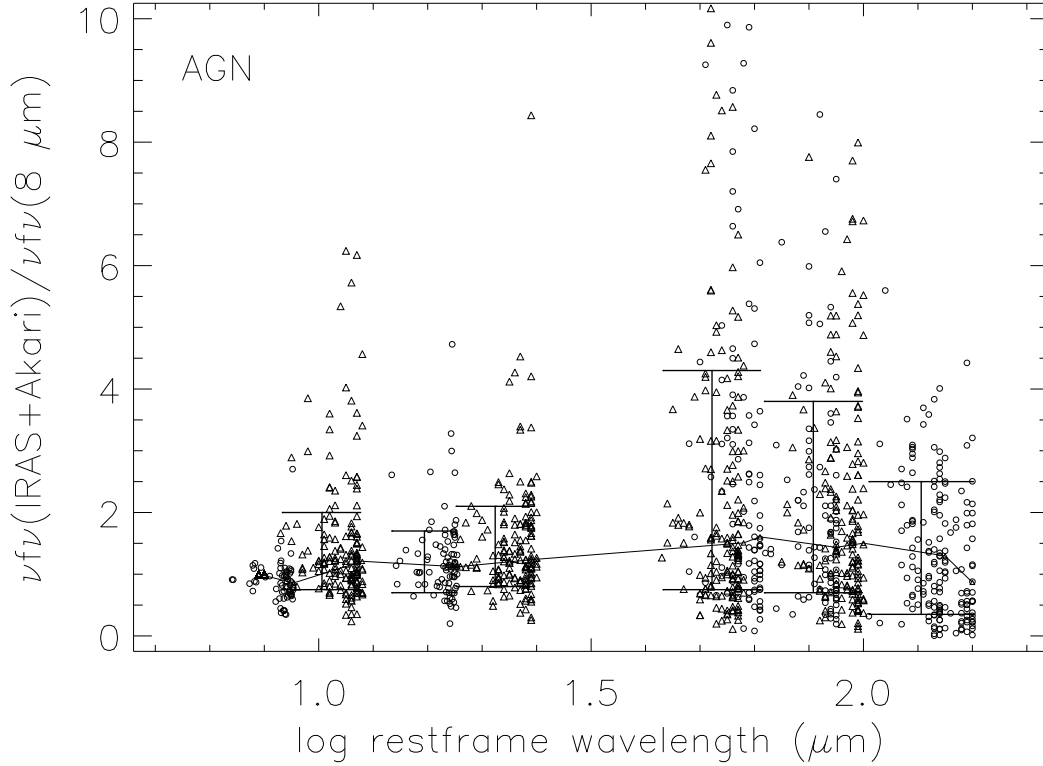


Fig. 11.— Spectral energy distributions for all AGN sources as determined from IRAS and AKARI flux densities, in the rest frame normalized to the peak $\nu f_{\nu}(\sim 8 \mu\text{m})$. Solid line shows medians at the observing wavelengths. Triangles are flux densities from IRAS, and circles are from AKARI. Observed points are at rest frame wavelengths and are distributed in wavelength because of different source redshifts. Error bars show one σ dispersions at the various rest frame wavelengths; dispersions are determined using combined points for $60 \mu\text{m}$ and $65 \mu\text{m}$, for $90 \mu\text{m}$ and $100 \mu\text{m}$, and for $140 \mu\text{m}$ and $160 \mu\text{m}$.

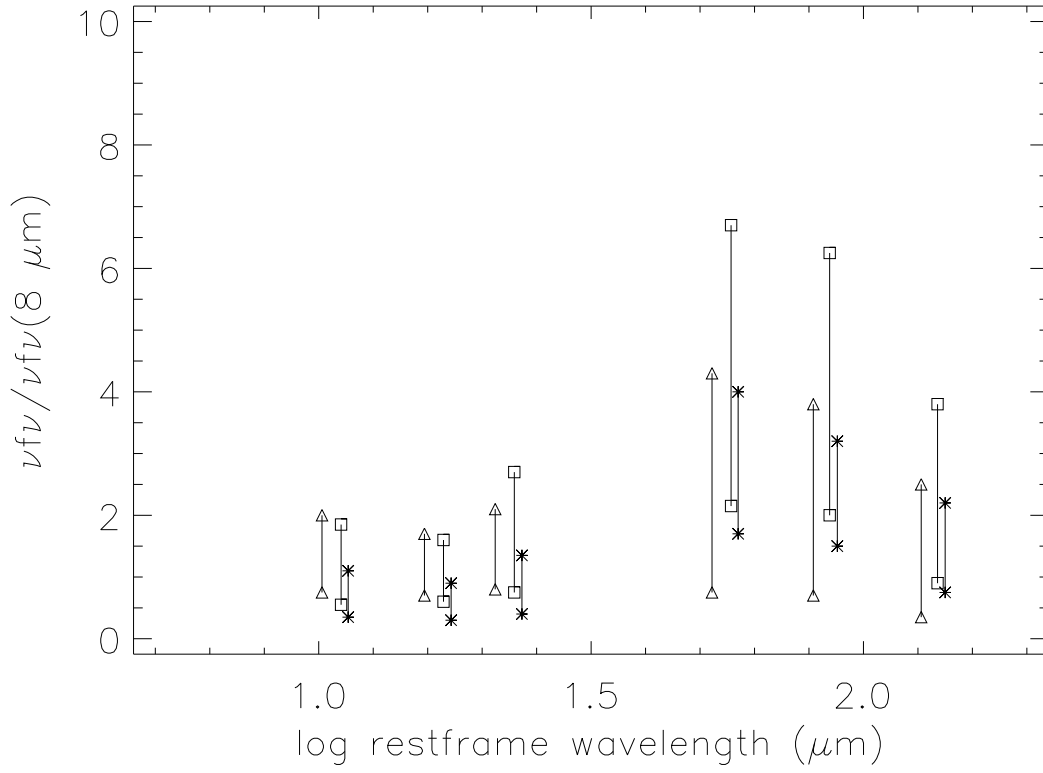


Fig. 12.— Dispersions for SEDs normalized to the peak νf_ν ($\sim 8 \mu\text{m}$) from Figures 9, 10, and 11 showing one σ dispersions at the various rest frame wavelengths. Asterisks are starbursts, squares are composites and triangles are AGN.

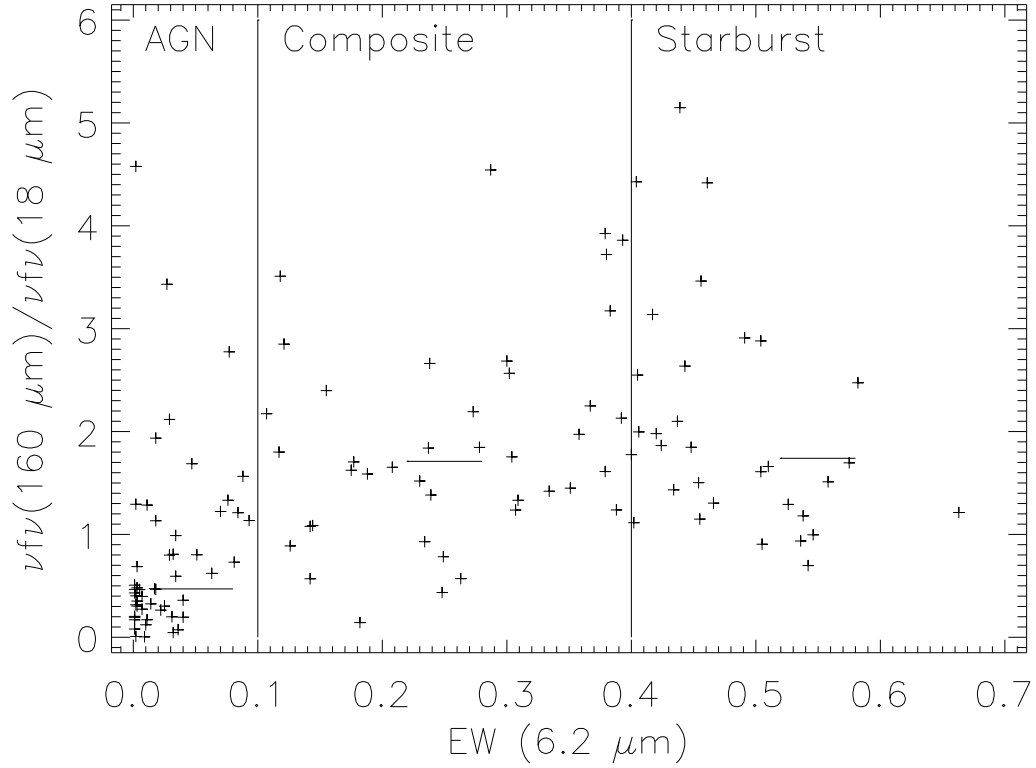


Fig. 13.— Comparison of cool dust component as measured by $\nu f_{\nu}(160 \mu\text{m})/\nu f_{\nu}(18 \mu\text{m})$ from AKARI fluxes with strength of starburst as measured by PAH $6.2 \mu\text{m}$ feature. Flux ratio shown is measure of relative luminosity in cooler dust radiating at $160 \mu\text{m}$ compared to warmer dust at $18 \mu\text{m}$. Quantitative change in ratio shows how starbursts have systematically cooler dust than AGN; median ratio for starbursts is 1.74, median for composites is 1.71, and median for AGN is 0.47, but the lower limit of this ratio for pure starbursts (0.7) is greater than the median for AGN (0.47).

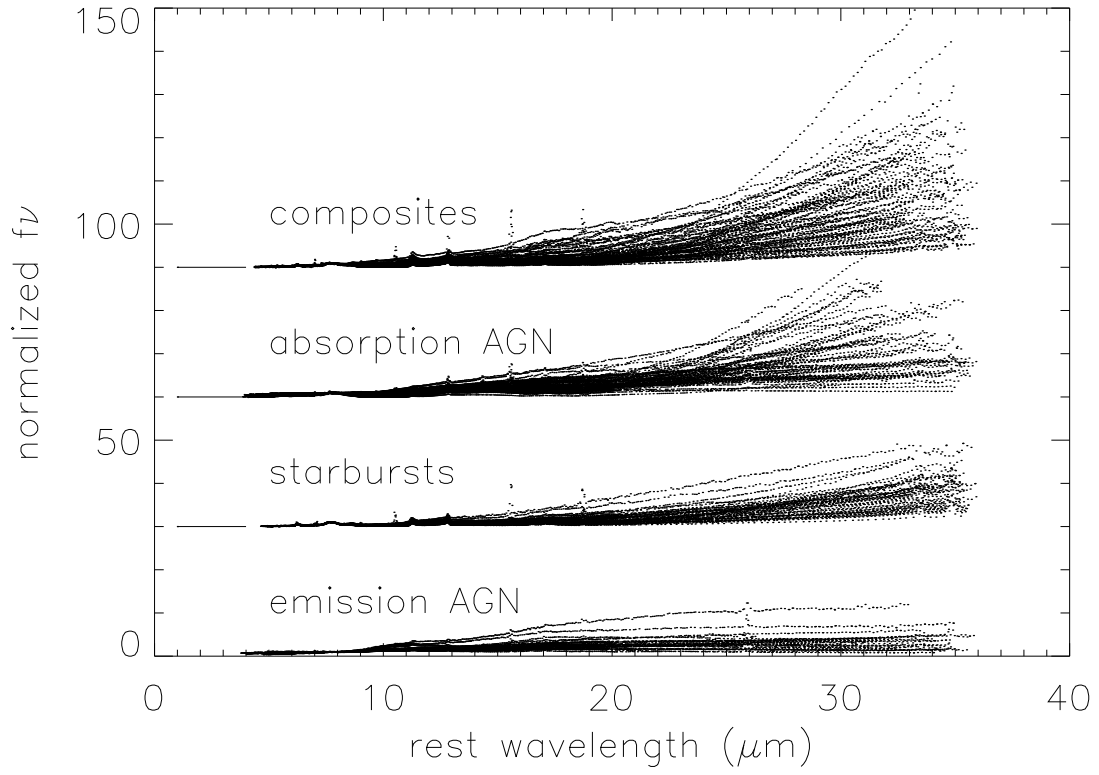


Fig. 14.— Spectra for all sources included in Tables 1-6, normalized to the peak f_ν ($\sim 8 \mu\text{m}$), with individual sources overlaid to show dispersion and extremes in rest frame spectra among the different categories. Zero levels of spectra are shown by short horizontal lines.

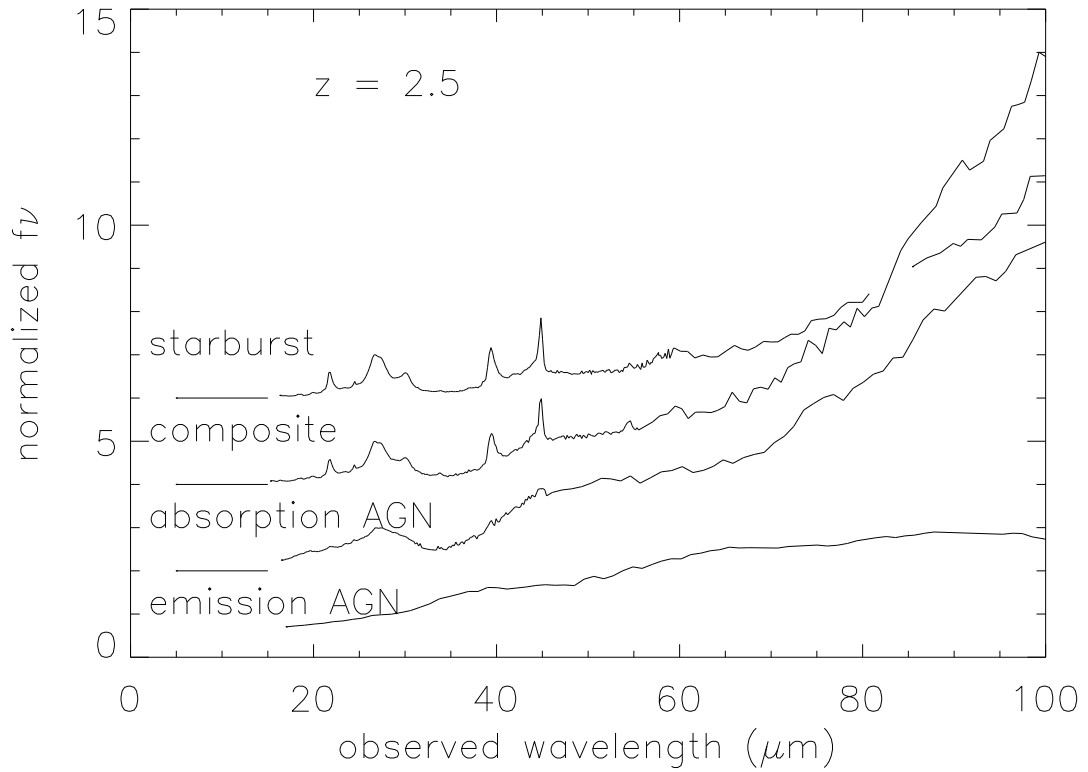


Fig. 15.— Average spectra for sources of different classifications in Tables 1-6, normalized to the peak f_ν ($\sim 8 \mu\text{m}$), as would appear in the observed frame if redshifted to $z = 2.5$. Spectra are offset by two units of f_ν for illustration. Zero levels of each spectrum are shown by short horizontal lines.